Follow-up surveillance of patients with cirrhosis has been performed to detect hepatocellular carcinoma (HCC) early enough to allow curative treatment (1). The American Association for the Study of Liver Diseases practice guidelines outline a strategy for distinguishing HCCs from other hepatic lesions of smaller than 3 cm that are identified during ultrasound (US) screening of livers in patients with cirrhosis (2). The guidelines suggest that nodules greater than 1 cm in diameter be further investigated by using dynamic contrast material–enhanced computed tomography (CT) or magnetic resonance (MR) imaging. Thus, the detection of arterial hypervascularization can justify treating the nodule as if it were HCC. For hypovascular nodules, defined as lesions that appear less enhanced than the surrounding liver both on arterial and venous phase images (2), careful monitoring (eg, repeat US at 3 months and biopsy) is recommended. However, the existing treatment guidelines do not specify the patient and tumor attributes that accurately predict subsequent hypervascularization.

Advances in Knowledge

- In patients with chronic liver disease, 31% (50 of 160) of the hypovascular nodules that showed hypointensity in the hepatobiliary phase of gadoxetic acid–enhanced MR imaging became hypervascular, which is a 1-year cumulative incidence of 25%.
- Hepatic hypovascular nodules that showed hyperintensity on T2-weighted images were at the highest risk for development of hypervascular hepatocellular carcinoma (hazard ratio, 8.7; 95% CI: 3.6, 20.8; $P < .001$).
- The higher growth rate (tumor volume doubling time, < 542 days) of a hepatic hypovascular nodule was associated with its subsequent development to hypervascular hepatocellular carcinoma.

The hepatobiliary phase of gadoxetic acid–enhanced MR imaging can allow clear visualization of hepatic focal lesions (3–6). Along with the widespread use of advanced imaging techniques, including three-dimensional T1-weighted gradient-echo sequences with high spatial resolution (7), hypovascular small nodules that show hypointensity on gadoxetic acid–enhanced hepatobiliary phase MR images are increasingly detected during HCC screening of patients with cirrhosis. Such nodules may include hypovascular well-differentiated HCCs, dysplastic nodules, and other benign nodules (8), which are difficult to distinguish, even at needle biopsy. Of these, hypovascular HCC and dysplastic nodules grow and acquire a more extensive arterial supply, and show overt stromal invasion (invasive growth of tumor tissue in portal tracts and fibrous septa), during stepwise carcinogenesis of HCC (9,10).

Previously, image-based studies suggested that hypovascular nodules containing fat or those that were greater than 10–15 mm in diameter were at high risk for development of hypervascularization (11–13). Authors of a histopathologic study (14) reported that most borderline nodules (dysplastic nodules or well-differentiated HCCs) greater than 15 mm in diameter were early HCC. Because these results were taken from findings at a single time point, further research examining the time course of the development of this change is required for the development of a better approach to follow-up of these hypovascular nodules.

Implications for Patient Care

- MR imaging findings may provide useful diagnostic information for the development of a treatment strategy for patients with hepatic hypovascular nodules.
- The hepatic hypovascular nodules that show hyperintensity on T2-weighted images, or that show a higher growth rate should be considered for more frequent follow-up or biopsy.

The aims of our study were to identify patient characteristics and MR imaging findings associated with subsequent hypervascularization in hypovascular nodules that show hypointensity on gadoxetic acid–enhanced hepatobiliary phase MR images in patients with chronic liver diseases.

Materials and Methods

Study Group

Retrospective data collection and analysis were approved by the institutional review board of the two participating hospitals, and the requirement for informed consent was waived. The selection of the subjects is outlined in Figure 1. From February 2008 to October 2010, there were 238 patients who underwent multiple gadoxetic acid–enhanced MR imaging examinations for HCC surveillance. Of these, we excluded patients with *(a)* Child-Pugh class C, owing to insufficient enhancement on gadoxetic acid–enhanced hepatobiliary phase MR images (1), and *(b)* those who had undergone previous systemic chemotherapy or treatment with molecularly targeted agents against malignant tumors. One radiologist (S. Kumano, with 22 years of experience in abdominal imaging) and one gastroenterologist

Published online
10.1148/radiol.12112677 **Content code:** GI

Radiology 2013; 266:480–490

Abbreviations:
CI = confidence interval
HCC = hepatocellular carcinoma
HR = hazard ratio
TVDT = tumor volume doubling time

Author contributions:
Guarantors of integrity of entire study, T.H., T. Murakami; study concepts/study design or data acquisition or data analysis/interpretation, all authors; manuscript drafting or manuscript revision for important intellectual content, all authors; approval of final version of submitted manuscript, all authors; literature research, T.H., Y.I., M.O., Y.K., S. Kumano, M.K., T. Murakami; clinical studies, T.H., Y.I., M.O., Y.K., S. Kogita, M.K.; statistical analysis, T.H., Y.I., M.H.; and manuscript editing, T.H., T. Murakami, Y.I., M.O., M.H., T. Mochizuki.

Conflicts of interest are listed at the end of this article.

Figure 1

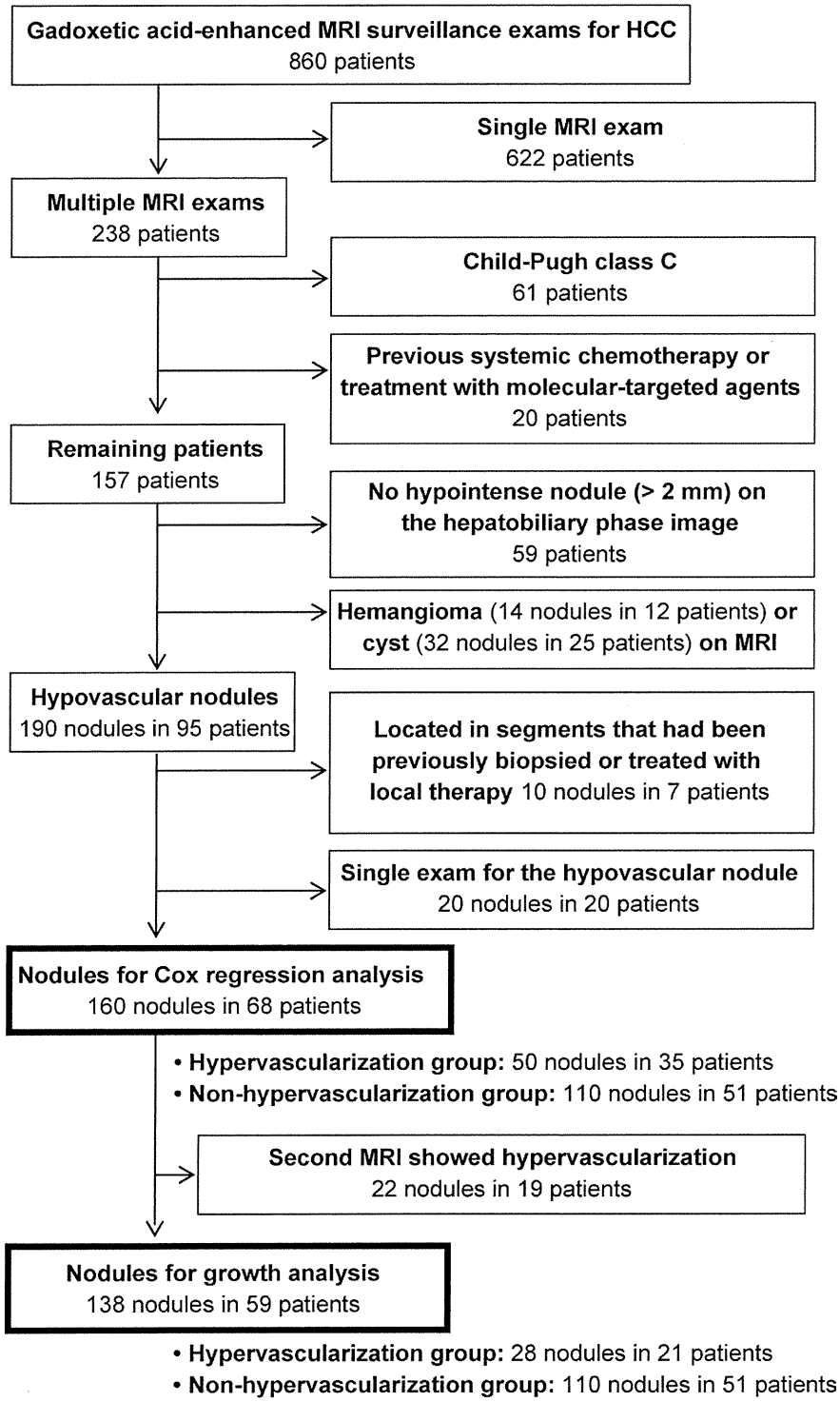

Figure 1: Flowchart of the study population.

specializing in hepatology (Y.I., with 30 years of experience) reviewed images to detect hypovascular nodules and to diagnose subsequent hypervascularization in consensus. A hypovascular nodule was defined as that in which all parts of the nodule showed lower signal intensity than the surrounding liver parenchyma during the arterial phase of dynamic imaging when any of the available modalities were used (intravenous contrast-enhanced CT, CT hepatic arteriography and contrast-enhanced ultrasound) compared with the corresponding site on the unenhanced image. The arterial enhancement was assessed by means of visual inspection. In addition, the subjects were limited to those with round hypointense lesions on gadoxetic acid–enhanced hepatobiliary phase MR images. Procedures involving all modalities were performed within 2 weeks of each other. Nodules were excluded if they were *(a)* less than 2 mm in diameter; *(b)* considered to be suspicious for hemangiomas, cysts or cystic tumors on the basis of other MR imaging sequences or modalities; or *(c)* located in segments that had been previously biopsied or treated with local therapy (including transcatheter arterial chemoembolization).

We identified 160 hypovascular nodules in 68 patients (mean patient age ± standard deviation, 70.0 ± 7.8 years; range, 51–85 years). Among these patients, 48 were men (mean age, 69.9 ± 7.7 years; range, 54–85 years), and 20 were women (mean age, 70.2 ± 8.4 years; range, 51–79 years). The presumed causes of chronic liver disease of the patients were chronic hepatitis C viral infection (n = 46), chronic hepatitis B viral infection (n = 12), alcohol abuse (n = 4), nonalcoholic steatohepatitis (n = 1) and unknown cause (n = 5). Forty (27%) patients had cirrhosis. The number of nodules per patient ranged from one to 10, with a mean value of 2.3. The date of entry into the study was defined as the date of the initial gadoxetic acid–enhanced MR imaging examination. All patients were treated according to the clinical guidelines for the diagnosis and treatment of HCC in Japan (15). During the study period, all patients

received follow-up gadoxetic acid–enhanced MR imaging examinations in combination with US, CT, or angiography at various times according to the degree of liver disease. One radiologist (S. Kumano) and one gastroenterologist who specializes in hepatology (Y.I.) reviewed images in consensus to verify lesion correspondence between the different imaging modalities. Each nodule was followed up until it showed early enhancement when imaged by means of any of the imaging modalities, until the segment containing the nodule was biopsied or treated, or until the final imaging examination of the study period. The number of gadoxetic acid–enhanced MR imaging examinations reviewed per patient was two for 32 patients (43%), three for 16 patients (28%), four for 12 patients (18%), five for three patients (4%), six for three patients (4%), seven for one patient (1%) and eight for one patient (1%). The mean interval between gadoxetic acid–enhanced MR imaging examinations was 186 days ± 110 (range, 57–619 days). Of the 110 nodules that did not develop into hypervascular nodules, 101 were censored at the date of the most recent consultation before November 1, 2010, and nine (in five patients) were censored at the date of the final imaging examination of the study period before therapy (six nodules for transarterial chemoembolization; one each for radiofrequency ablation, intra-arterial reservoir chemotherapy and whole-liver radiation therapy due to coexistent HCC) of the liver segment(s) involved.

We obtained the baseline clinical data by means of review of all available medical records for assessment of the association with the subsequent hypervascularization. The clinical data comprised seven patient characteristics at the time of baseline MR imaging and six initial gadoxetic acid–enhanced MR imaging findings from each nodule (see the Imaging Analysis subsection). Patient characteristics that were used in the study were age, sex, Child-Pugh classification, cause of liver disease, serum α-fetoprotein level, history of local therapy for HCC, and coexistence of hypervascular HCC. For patients with hepatitis B infections, we recorded information regarding the use of oral nucleotide analogs with activity against hepatitis B. The mean interval between the laboratory test and initial MR imaging examination was 9 days (range, 0–24 days).

Nodules were categorized into two groups according to the presence (hypervascularization group) or absence (nonhypervascularization group) of early enhancement at the final imaging examination. Needle biopsy specimens were reviewed by two expert pathologists who made a consensus diagnosis according to the International Working Party criteria (9).

Imaging Techniques

MR imaging studies were performed by using either a 3.0 T (Achieva; Philips Medical Systems, Best, Netherlands) or one of two 1.5 T systems (Signa Excite HDxt; GE Healthcare, Milwaukee, Wis; Gyroscan Intera Nova; Philips Medical Systems) (Table 1). First, a T1-weighted dual-echo sequence was performed. For dynamic imaging, T1-weighted three-dimensional fat-suppressed gradient-echo images were acquired before and after a bolus injection of 0.025 mmol/kg of body weight of gadoxetic acid (EOB-Primovist; Bayer Schering Pharma, Osaka, Japan) at a rate of 2 mL/sec with a saline flush through the antecubital vein. Arterial-phase imaging was performed by using a bolus tracking technique: the center of k-space was acquired 15 seconds after the contrast material appeared in the abdominal aorta (16). Portal venous and hepatobiliary phase images were acquired after an imaging delay of 70 seconds and 20 minutes, respectively. T2-weighted images were acquired with a fat-suppressed fast spin-echo sequence before or within 10 min after contrast-material injection. Although there were missing data from the fat-suppressed T2-weighted fast spin-echo images (not available owing to motion artifacts in two nodules; other T2-weighted sequences were obtained for 32 nodules), we included all subjects in the analysis. Dynamic contrast-enhanced CT, CT hepatic arteriography and contrast-enhanced US were performed as described in the literature (17–19).

Image Analysis

A consensus review of baseline MR images was performed by three radiologists (M.O., T.H., and Y.K., with 18, 11, and 6 years of experience in abdominal imaging, respectively), who were blinded to the outcomes and the biopsy results for each nodule. The fat content of each nodule was determined on the basis of T1-weighted dual-echo images according to apparent signal loss on opposed-phase images relative to in-phase images. On the T2-weighted images, each lesion was evaluated for signal intensity relative to that of the surrounding liver parenchyma and classified as hyperintense, isointense, hypointense or missing. On the T1-weighted three-dimensional fat-suppressed gradient-echo images of without and with contrast enhancement (hepatobiliary phase), signal intensities of the nodule and liver parenchyma were recorded to evaluate nodule-to-liver contrast ratios. For measurement of the nodule, one abdominal radiologist (T.H.) placed the largest possible region of interest but did not include the edges of the nodule to avoid edge artifacts. For the liver parenchyma, two regions of interest that avoided the major hepatic and portal vessels (size range, 200–400 mm^2) were selected, and then the mean value was calculated. The nodule-to-liver contrast ratios were calculated for each unenhanced and hepatobiliary phase image by dividing the signal intensity of the nodule by the signal intensity of the liver parenchyma. The contrast enhancement ratio was then calculated by dividing the contrast ratios of the hepatobiliary phase images by those of the unenhanced images.

One abdominal radiologist (T.H.) measured the maximum nodule diameter on axial gradient-echo T1-weighted gadoxetic acid–enhanced hepatobiliary-phase images of the baseline and the final MR imaging examinations. Only for the purpose of the growth analysis, the final MR imaging examination was defined as the last MR imaging examination before hypervascularization for each nodule. Twenty-two nodules in which the second MR imaging examination showed hypervascularization (19 pairs of examinations; median interval between the two examinations, 210 days;

Table 1

Pulse Sequence Parameters for 1.5-T and 3.0-T Imaging

	T1-weighted Dual-Echo GRE*		Fat-suppressed 3D T1-weighted GRE		Fat-suppressed T2-weighted Fast Spin-Echo	
Parameter	1.5 T 2D†	3.0 T 3D‡	1.5 T†	3.0 T‡	1.5 T†	3.0 T‡
Breathing	Breath hold	Breath hold	Breath hold	Breath hold	Respiratory-triggered technique	Respiratory-triggered technique
Matrix	256 × 256, 320 × 192	192, 176	320 × 512, 320 × 192	320 × 256, 320 × 192	512 × 272, 256 × 224	400, 400
Section thickness (mm)	8, 3.5	7, 7	5, 5	2.5, 3	8, 7	6, 6
Intersection gap (mm)	0.8, 0	0, 0	−2.5, −2.5	−1.25, −1.5	0.8, 1.4	1, 1
Repetition time (msec)	200, 200	3.9, 3.8	4.4, 4.3	3.5, 3.5	>2000, >2000	>3000, >3000
Echo time (msec) in/opposed	4.6/2.3, 4.3/2.1	1.17/2.5, 1.17/2.5	2.2, 2.1	1.7, 1.7	80, 105	80, 80
Flip angle/refocusing angle (degrees)	70, 70	10, 10	10, 12	10, 10	180, 180	160, 160
Reduction factor	1.8, 2	2, 2	1.8, 2	2, 1.9	0, 2	1.6, 2

Note.—Field of view was 250–270 mm × 350–380 mm (adjusted for each patient). 2D = two dimensional, 3D = three dimensional, GRE = gradient-recalled echo.

* Indicates in- and opposed-phase imaging.

† For the 1.5-T system, a 16-channel and an 8-channel phased-array body coil were used. Data are presented as 16 channel/8 channel.

‡ For the 3-T system, a 6-channel body coil and 32-channel cardiac coil were used and adjusted to the patient's physique. Data are presented as 6 channel/32 channel.

range, 91–410 days) were excluded from the growth analysis, because the growth rate before hypervascularization could not be calculated. Thus, 138 nodules from 59 patients were included in the growth analysis. First, the tumor volume doubling time (TVDT) was calculated as follows (20,21): TVDT = $T \times \log 2/[3 \times \log(D_2/D_1)]$, where T is the time interval between two measurements and D_1 and D_2 denote the maximum diameter of the nodule at the initial and last MR imaging examinations, respectively. Then, the growth rate of the nodules was calculated as the inverse of the TVDT.

Statistical Analysis

All analyses were conducted at the nodule level. R software (Version 2.12.0; R Foundation for Statistical Computing, Vienna, Austria) was used for statistical analysis (22). To evaluate the independent prognostic significance of baseline covariates for subsequent hypervascularization, a multivariate Cox proportional hazard model was used. Because 32 patients had multiple nodules detected at two or more follow-up examinations, we used the coxph function from the survival package in the R software, with the cluster option. This method allows accounting for correlation induced by having multiple nodules per patient and uses robust variance estimates (23). Before model selection, bivariate analysis was performed by using Spearman rank correlations to test for collinearity among independent variables. As a result, Spearman correlation coefficients for variables were generally below 0.5, which suggests that multicollinearity was not of concern. Hazard ratios (HRs) and 95% confidence intervals (CIs) were calculated. Because no factor (except intensity on T2-weighted images) was found to show a significant difference when univariate analysis was performed, preliminary multivariate Cox proportional hazards models were constructed by using all 13 variables. Candidate variables were then allowed to enter the final model (entry criterion, $P < .05$). Fat content and initial diameter were forced into the final model because they were considered important predictors (12). The Wald test was performed to determine an overall P value for each variable, and a robust score test was used to assess the significance of the final model as a whole. The model that was fitted by using missing data was not appreciably different from that with the missing data excluded.

The median time interval between the initial and final MR imaging examination was compared for the two groups by using the Mann-Whitney U test. For evaluation of initial diameter and growth rate of the nodules, continuous data differences between the two groups were tested with the Mann-Whitney U test, and categorical data were assessed by using the χ^2 test. Correlation between the initial diameter and the growth rate of the nodules was examined by using the Kendall tau rank test. The prognostic value of the growth rate was evaluated by means of the area under the receiver operating characteristic curve. By using the ROCR package in the R software, the cutoff value for the growth rate was determined at the optimal operating point, with the highest sensitivity and specificity combined (24). Cumulative event rates were estimated by using the Kaplan-Meier method and compared by using the log rank statistic. A P value of less than .05 was considered to indicate a statistically significant difference. All P values were two-sided.

Results

Study Population and Events

During the median follow-up time of 342 days (range, 64–948 days), arterial hypervascularization was observed in 31% (50 of 160) of the nodules in 52% (35 of 68) of the patients. The cumulative percentages of nodules that showed

Table 2

Baseline Patient Characteristics and MR Imaging Findings of 160 Nodules

Parameter	No. of Nodules	Hypervascularization at Follow-up		Preliminary Multivariate Cox Model	
		Yes ($n = 50$)	No ($n = 110$)	HR (95% CI)	*P* Value
Patient characteristic					
Age (y)	...	70.5 ± 7.6 (58–85)*	70.4 ± 8.3 (51–84)*	1.0 (0.9, 1.1)	.852
Sex	...				.326
Men	106	32 (30)	74 (70)	1.0	
Women	54	18 (33)	36 (67)	1.4 (0.7, 3.1)	
Child-Pugh class					.005
A or chronic hepatitis	146	44 (30)	102 (70)	1.0	
B	14	6 (43)	8 (57)	3.8 (1.5, 9.0)	
Etiology of liver disease					.019
Hepatitis C virus	107	35 (33)	72 (67)	1.0 (0.3, 3.1)	
Hepatitis B virus	26	6 (23)	20 (77)	0.2 (0.03, 0.8)	
Non-B, non-C (ref)	27	9 (33)	18 (67)	1.0	
Serum α-fetoprotein level > 20 ng/mL	66	24 (36)	42 (64)	0.9 (0.5, 2.0)	.948
History of local therapy for HCC	129	46 (36)	83 (64)	5.5 (2.1, 14.7)	<.001
Coexistence of hypervascular HCC	67	29 (43)	38 (57)	2.0 (1.1, 3.7)	.022
MR Imaging Finding					
Fat-suppressed T2-weighted fast spin echo†					<.001
Hyperintensity	18	10 (56)	8 (44)	9.4 (3.6, 24.5)	
Iso- or hypointensity (ref)	108	25 (23)	83 (77)	1.0	
Missing data	34	15 (34)	19 (56)	3.7 (1.7, 8.0)	
Fat containing on in- and opposed-phase images†	24	10 (42)	14 (58)	1.4 (0.6, 3.4)	.491
Noise-to-liver contrast on unenhanced fat-suppressed T1-weighted GRE images	...	0.95 ± 0.14 (0.66–1.3)*	0.97 ± 0.17 (0.49–1.9)*	0.05 (0.1×10^{-4}, 1.7×10^{2})	.464
Noise-to-liver contrast on hepatobiliary phase fat-suppressed T1-weighted GRE images	...	0.69 ± 0.13 (0.31–0.99)*	0.71 ± 0.11 (0.46–0.95)*	47.5 (6.8×10^{-4}, 3.3×10^{6})	.489
Gadoxetic acid contrast-enhancement ratio	...	0.74 ± 0.14 (0.40–0.98)*	0.75 ± 0.14 (0.42–1.5)*	0.07 (0.1×10^{-5}, 3.8×10^{3})	.629
Diameter (mm)	...	9.5 ± 5.1 (2–34)*	9.8 ± 3.7 (4–21)*	1.0 (0.9, 1.1)	.998

Note.—Unless otherwise indicated, data are numbers of patients, with percentages in parentheses. GRE = gradient-recalled echo, ref = referent category.

* Data are mean ± standard deviation, with range in parentheses.

† Qualitative assessment.

hypervascularization at 6, 12, 18, and 24 months were 10%, 25%, 36%, and 46%, respectively. Hypervascularization was diagnosed in 39 nodules on the basis of arterial-phase gadoxetic acid–enhanced MR images, eight nodules on the basis of dynamic CT images, two nodules on the basis of CT hepatic arteriographic images, and one nodule on the basis of contrast-enhanced US. In the hypervascularization group, the mean number of hypervascularized nodules was 1.5 (range, 1–7) per patient during the study period.

Histologic results from core needle biopsy were obtained for 13 nodules. Of these, nine nodules were in the hypervascularization group (eight well-differentiated HCCs and one moderately differentiated HCC). Three nodules in the nonhypervascularization group were diagnosed as dysplastic nodules and one as well-differentiated HCC.

Baseline Findings

Table 2 shows the baseline characteristics of the 160 nodules and results of the preliminary multivariate Cox regression. In the final model, five of the variables showed a statistically significant difference (robust score test, $P = .023$; Table 3). The factors associated with an increased risk of hypervascularization were hyperintensity on T2-weighted images (HR = 8.7; 95% CI: 3.6, 20.8), previous local therapy for HCC (HR = 5.0; 95% CI: 1.8, 13.6), Child-Pugh class B cirrhosis (HR = 3.6; 95% CI: 1.4, 9.5), and coexistence of hypervascular HCC (HR = 2.0; 95% CI: 1.0, 3.8). Hepatitis B infection was independently associated with a decreased risk (HR = 0.2; 95% CI: 0.04, 0.8). Of 26 nodules in 13 patients with chronic hepatitis B infections, 23 nodules in 11 patients were treated with oral nucleotide analogs with activity against hepatitis B at the point of entry (five of six nodules in the hypervascularization group and 18 of 20 nodules in the nonhypervascularization group). Fat content and the initial diameter of the nodule were not substantially different in the final model. Of 14 fat-containing nodules in the nonhypervascularization

group, four nodules in one patient were censored because the patient underwent transcatheter arterial chemoembolization for HCC in a different liver segment. Two nodules were censored because of biopsy; one was diagnosed as moderately differentiated HCC, and the other was a dysplastic nodule. The mean initial nodule diameter was not significantly different between the hypervascularization (9.5 mm ± 5.1 [range, 2–34 mm]) and the nonhypervascularization groups (9.8 mm ± 3.7 [range, 4–21 mm]) (P = .282). The numbers of nodules that were smaller than 5 mm, 5–10 mm, 10–15 mm, and greater than 15 mm in initial size were four, 28, 11, and seven in the hypervascularization group, and three, 60, 33, and 14 in the nonhypervascularization group, respectively. In addition, there was no difference in the percentage of nodules greater than or equal to 15 mm in size between the two groups (14% [seven of 50] vs 13% [14 of 110], respectively; P = .825).

Table 3

Multivariate Predictors of Subsequent Hypervascularization

Variable	HR (95% CI)	*P* Value
Significant independent predictors		
Child-Pugh classification		.008
A or chronic hepatitis	1.0	
B	3.6 (1.4, 9.5)	
Cause of liver disease		.017
Hepatitis C virus	1.1 (0.4, 3.1)	
Hepatitis B virus	0.2 (0.04, 0.8)	
Non-B and non-C liver disease (Ref)	1.0	
History of local therapy for HCC	5.0 (1.8, 13.6)	.002
Coexistence of hypervascular HCC	2.0 (1.0, 3.8)	.038
Fat-suppressed T2-weighted fast spin echo		<.001
Hyperintensity	8.7 (3.6, 20.8)	
Hypo- or isointensity (Ref)	1.0	
Missing data	3.4 (1.4, 7.9)	
Additional variables included in the model		
Fat containing on in- and opposed-phase images	1.3 (0.5, 3.7)	.567
Diameter (mm)	1.0 (0.9, 1.1)	.692

Growth Analysis

Twenty-eight lesions in the hypervascularization group (initial diameter, 9.7 mm ± 5.9 [range, 2–34 mm]) and 110 nodules (9.8 mm ± 3.7 [range, 4–21 mm]) in the nonhypervascularization group were evaluated. The median time between the initial and last MR imaging examination was not significantly different (P = .075) between the two groups (235 and 293 days, respectively). In the hypervascularization group, 27 nodules increased in diameter during follow-up (Fig 2) and one remained stable. The mean growth rate in the hypervascularization group (6.5×10^{-3}/day [TVDT, 154 days]) was significantly higher ($P = 1.8 \times 10^{-6}$) than that in the nonhypervascularization group (1.1×10^{-3}/day [TVDT, 946 days]) (Fig 3). There was no correlation between initial diameter and growth rate (Kendall tau = −0.066; P = .266) (Fig 4). Receiver operating characteristic analysis (area under the curve, 0.79) identified a growth rate cutoff value of 1.8×10^{-3} per day (TVDT, 542 days) with a positive predictive value of 89% (25 of 28 nodules) and a negative predictive value of 63% (70 of 110 nodules) for hypervascularization (Fig 5, *A*). The 1-year cumulative proportion of nodules showing hypervascularization was 0% for those with a growth rate of less than 1.8×10^{-3}/day and 53% for those with a growth rate greater than or equal to 1.8×10^{-3}/day (log-rank test, $P = 5.2 \times 10^{-8}$; Fig 5, *B*).

Discussion

We set out to determine risk factors associated with hypervascularization in hypovascular nodules in patients with chronic liver diseases by using time-to-event analysis. Among the baseline patient characteristics and MR imaging findings, the most important variable associated with an increased risk of hypervascularization was hyperintensity on T2-weighted images. In the hypervascularization group, higher signal intensity on T2-weighted images might reflect peliotic changes in the intratumoral sinusoids of HCC (25). Meanwhile, nodular regeneration, fibrosis, and scarring that occur in the course of cirrhosis occasionally appear as hyperintense round lesions on T2-weighted images. Dysplastic nodules can be hyperintense on T2-weighted images; the causes are considered to be varying degrees of fibrosis, or infarction (26,27). It has been reported that T2-weighted imaging does not provide added diagnostic value to gadoxetic acid–enhanced images for the detection and characterization of focal lesions in cirrhotic livers (28). Findings from our study suggest that the combination of T2-weighted images and gadoxetic acid–enhanced MR images could be useful in the prediction of hypervascularization of previously hypovascular nodules.

Child-Pugh class B cirrhosis increased the risk of hypervascularization compared with Child-Pugh class A or chronic hepatitis, and hepatitis B infection decreased the risk compared with hepatitis C infection. These results might reflect the epidemiologic features of HCC (29,30); Child-Pugh class B and C are associated with a three-fold increase in the risk of HCC. The annual incidence of HCC in patients with cirrhosis due to hepatitis B infection exceeds 2%, which is lower than that due to hepatitis C infection (3%–8%). In addition, there may be morphologic and histologic differences between hypovascular nodules associated with hepatitis B and those associated with hepatitis C infection.

Figure 2

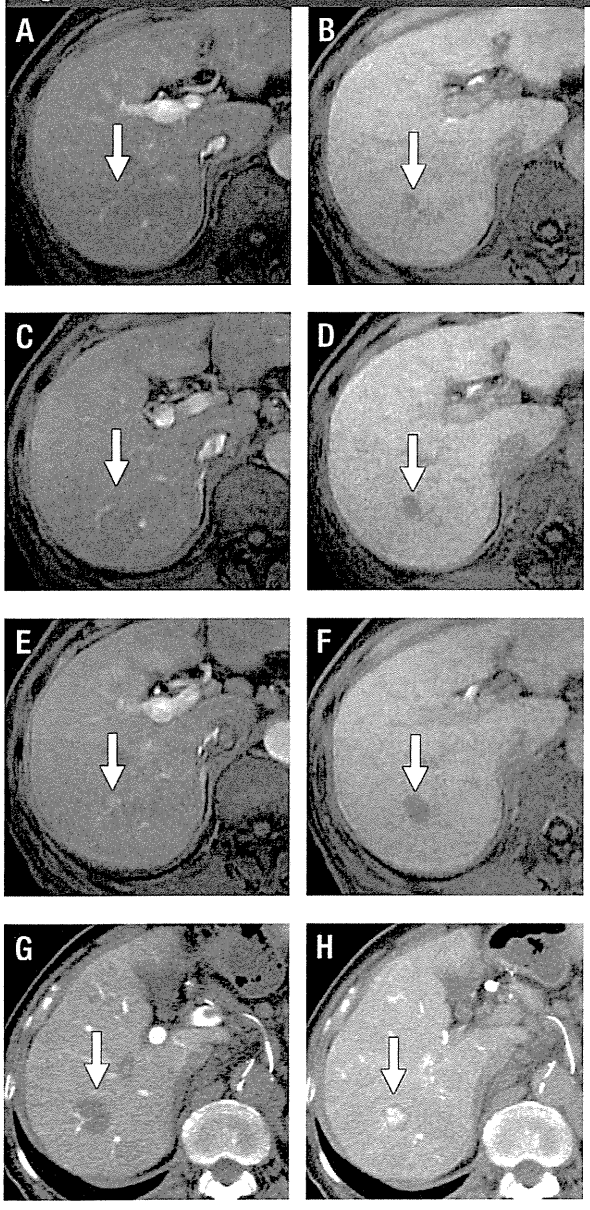

Figure 2: Growing hypovascular hepatic nodule (arrows) and subsequent hypervascularization in an 86-year-old man with hepatitis C and Child-Pugh class B cirrhosis. *A-F*, Axial gadoxetic acid–enhanced T1-weighted fat-suppressed three-dimensional gradient-recalled echo images obtained during (*A*, *C*, and *E*) arterial phase and (*B*, *D*, *F*) hepatobiliary phase obtained at (*A*, *B*) baseline, (*C*, *D*) day 94, and (*E*, *F*) day 176. At (*A*) baseline and (*C*) day 94, hepatic nodule in right posterior section showed neither arterial-phase enhancement nor portal-venous phase washout. Hepatobiliary phase images showed that maximum diameter increased from 8 mm at, *B*, baseline to 12 mm at, *D*, day 94, and TVDT was calculated as 170 days. *E*, Arterial-phase image at day 176 shows partial enhanceme of nodule. *G*, At day 194, CT arterial portographic image shows a well-defined, round perfusion defect and, *H*, CT hepatic arteriographic image shows marked enhancement corresponding to nodule. Nodule was diagnosed as HCC on the basis of image views and tumor markers.

Figure 3

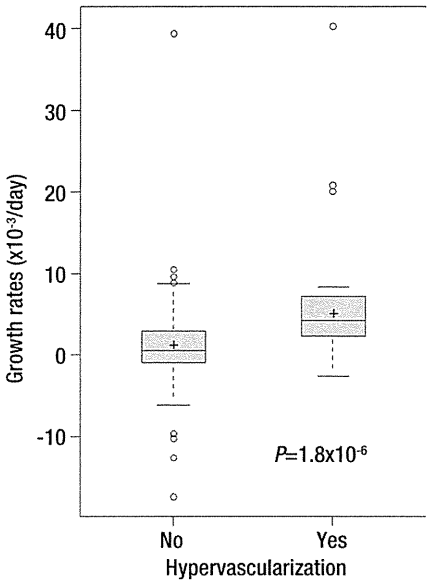

Figure 3: Box plot shows distribution of growth rates of 138 nodules. Median values and 25th and 75th percentiles are shown in each box plot. Vertical bars represent largest and smallest values that are not outliers. + = Mean; ○ = outlier of more than 1.5 times box length.

In comparison with hepatitis C infection or alcohol abuse, hepatitis B infection tends to induce macronodular (> 3 mm) cirrhosis (31). Thus, macronodular benign nodules in cases of hepatitis B cirrhosis might have been present in our subjects. Another possible reason why hepatitis B infection was a negative predictor for hypervascularization might be that antihepatitis B nucleoside analogs prevented the development of HCC (32).

The nodule-to-liver contrast ratios on unenhanced T1-weighted images and gadoxetic acid–enhanced hepatobiliary phase MR images were not a significant prognostic factor, which is consistent with previous reports (33). The signal intensity of nodules on T1-weighted images may be affected by intratumoral fat, metal, or glycogen in the surrounding hepatic parenchyma (1,34). The fat content of the nodules was also not a significant predictor of hypervascularization in our study. One possible reason for this was the fact that both early HCCs and dysplastic nodules could appear as intracellular lipid-containing lesions in cirrhotic livers (35). There was also no statistically significant association between initial diameter and hypervascularization in our study results. The probable reason for this was that most subjects (87%) had nodules of less than 15 mm in diameter (139 of 160 nodules).

The reported TVDT for HCC ranges from 18 to 605 days (1). The mean growth rate for HCCs smaller than 20 mm that showed no hyperintensity on T2-weighted MR images but that enhanced during arterial phase MR imaging was 10.5×10^{-3}/day (TVDT, 95 days; calculated by using data from Jeong et al [36]). The hypervascularization group, which was considered to be representative of an earlier stage of multistep carcinogenesis, showed the lower mean growth rate (6.5×10^{-3}/day [TVDT, 154

Figure 5

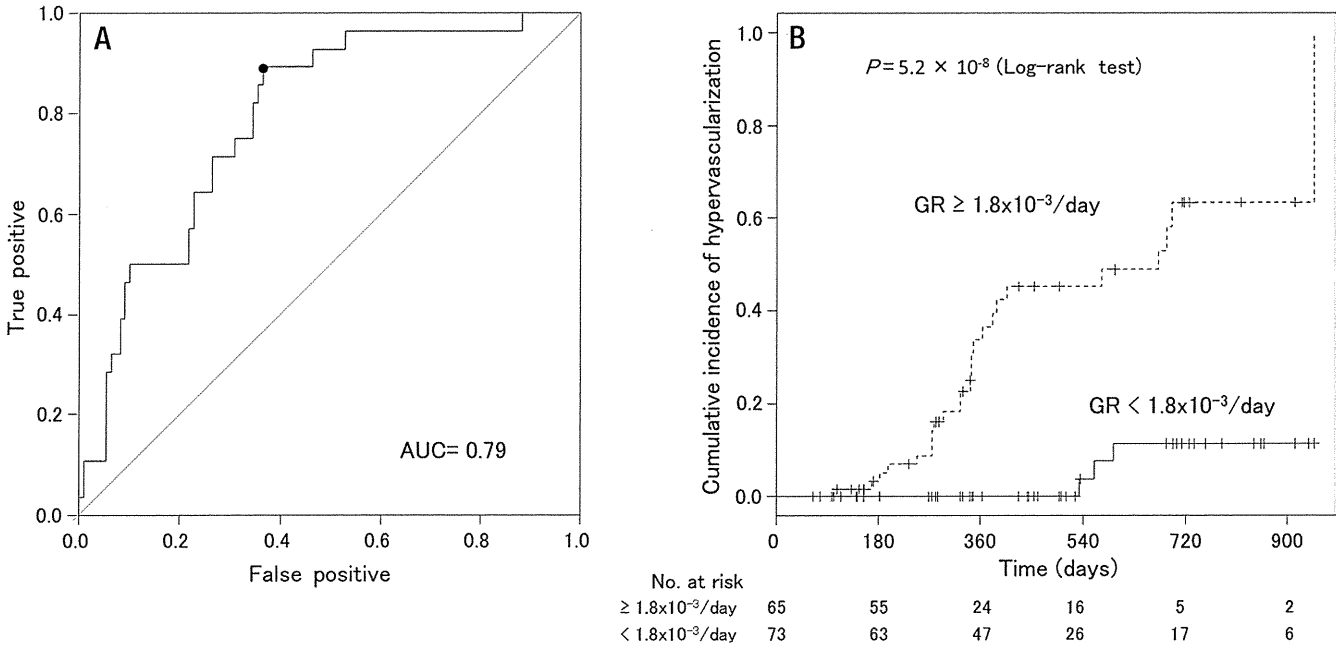

Figure 5: *A*, Graph shows receiver operating characteristic curve of growth rate *(GR)* for the prediction of hypervascularization (area under the curve *[AUC]*, 0.79). The optimal operating point on the receiver operating characteristic curve is marked with a black dot (growth rate, 1.8 × 10^{-3}/day). *B*, Kaplan-Meier analysis shows effect of growth rate on cumulative incidence of hypervascularization. Number of nodules at risk at each time point is shown at bottom of figure.

days]) than that reported in the Jeong et al study (36).

On the basis of these previous studies, hypovascular nodules larger than 15 mm are considered appropriate for biopsy. In cases with nodules less than 10 mm in diameter, the American Association for the Study of Liver Disease recommends imaging follow-up at 3–6 month intervals, with careful attention to increases in size or changes in vascular pattern. Repeated biopsy for nodules larger than 10 mm can be performed, but a needle liver biopsy has some disadvantages including inaccurate sampling caused by technical difficulties (eg, poor lesion or needle visualization, deeply located lesions, and hepatic fibrosis), risk of bleeding, and needle track seeding. Our growth analysis, along with baseline risk factors, might improve diagnostic discrimination with or without the need for biopsy, particularly for nodules measuring 10–15 mm. By using a cutoff growth rate of 1.8 × 10^{-3}/day (TVDT, 542 days), the calculated diameters at

Figure 4

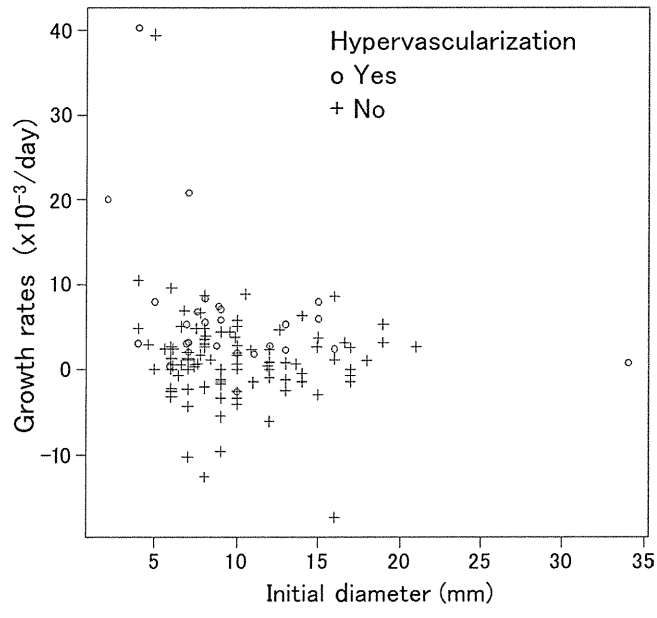

Figure 4: Scatterplot shows growth rate above the initial diameter. Individual nodules were coded according to whether they showed subsequent hypervascularization during the study period.

the 6-month follow-up examination for nodules with an initial diameter of 10, 11, 12, 13, and 14 mm were 10.8, 11.9, 13.0, 14.0, and 15.1 mm, respectively. We suggest that nodules with the risk factors for hypervascularization or those showing faster growth may justify more frequent follow-up or biopsy. If growth is slower, biopsy may not be needed, although the absence of growth does not rule out malignancy. According to expert opinion, nodules are declared benign only if they regress or remain stable for 2 years (37).

The reported incidence rates of hypervascularization vary throughout different studies. In our study, the overall 6- and 12-month cumulative percentages for hypervascularization were 10% and 25%, respectively, which is lower than the percentages calculated by Kumada et al (27.6% and 43.5%, respectively) (13). This may be partially explained by time frame, sample size, and/or follow-up policy of subjects in each study.

Our study had some limitations. It was a retrospective study, and this fact may have introduced bias in data homogeneity. To minimize sampling bias, we collected data from consecutive patients who underwent multiple gadoxetic acid–enhanced MR imaging examinations in two hospitals. Also, the duration of disease and date of diagnosis were potentially important confounders. However, they were not available for retrospective review.

Regarding the imaging technique, a relatively high rate (2 mL/sec) of injection of gadoxetic acid might reduce the performance of arterial-phase imaging. Some reports suggested that a lower injection rate might be appropriate owing to stretching the bolus without reducing the enhancement peak (38,39). However, we performed gadoxetic acid–enhanced MR imaging with optimized imaging technique (40) and timing (16) to acquire good images in the arterial phase.

On imaging analysis, our study was potentially limited by consensus review because we did not assess interobserver variability. Also, in the case of smaller nodules (< 10 mm), it might be difficult to obtain a clear correspondence between the MR images and those of the other modalities (CT, and in particular, contrast-enhanced US), even though well-trained radiologists and physicians reviewed the images.

Tumor growth kinetic calculations were based on the general assumption that tumor cells grow exponentially. This assumption might not hold true owing to fibrosis or to the intracellular lipid content of both the hepatic nodules and surrounding cirrhotic liver parenchyma. Because patients with Child-Pugh class C cirrhosis were excluded, the influence of fibrosis of the surrounding parenchyma is limited. Also, measurement errors associated with manual evaluation may have led to bias. However, to improve accuracy all measurements were performed in the same manner, by using T1-weighted three-dimensional gradient-echo images that provided high spatial resolution (7). A large-scale prospective validation study is necessary to confirm our proposed cutoff values.

In conclusion, hypervascularization occurs in about one-third of the hypovascular nodules that show hypointensity on gadoxetic acid–enhanced hepatobiliary phase MR images. MR imaging findings, including hyperintensity on T2-weighted images and a higher growth rate, may predict arterial hypervascularization, which may lead to early diagnosis and treatment of HCC.

Disclosures of Conflicts of Interest: T.H. Financial activities related to the present article: Received Osaka Cancer Foundation grant in 2010. Financial activities not related to the present article: none to disclose. Other relationships: none to disclose. **T. Murakami** No relevant conflicts of interest to disclose. **Y.I.** No relevant conflicts of interest to disclose. **M.O.** No relevant conflicts of interest to disclose. **M.H.** No relevant conflicts of interest to disclose. **Y.K.** No relevant conflicts of interest to disclose. **S. Kogita** No relevant conflicts of interest to disclose. **S. Kumano** No relevant conflicts of interest to disclose. **M.K.** No relevant conflicts of interest to disclose. **T. Mochizuki** No relevant conflicts of interest to disclose.

References

1. Willatt JM, Hussain HK, Adusumilli S, Marrero JA. MR Imaging of hepatocellular carcinoma in the cirrhotic liver: challenges and controversies. Radiology 2008;247(2):311–330.
2. Bruix J, Sherman M; American Association for the Study of Liver Diseases. Management of hepatocellular carcinoma: an update. Hepatology 2011;53(3):1020–1022.
3. Giovagnoni A, Paci E. Liver. III: Gadolinium-based hepatobiliary contrast agents (Gd-EOB-DTPA and Gd-BOPTA/Dimeg). Magn Reson Imaging Clin N Am 1996;4(1):61–72.
4. Bluemke DA, Sahani D, Amendola M, et al. Efficacy and safety of MR imaging with liver-specific contrast agent: U.S. multicenter phase III study. Radiology 2005;237(1):89–98.
5. Haradome H, Grazioli L, Tinti R, et al. Additional value of gadoxetic acid-DTPA-enhanced hepatobiliary phase MR imaging in the diagnosis of early-stage hepatocellular carcinoma: comparison with dynamic triple-phase multidetector CT imaging. J Magn Reson Imaging 2011;34(1):69–78.
6. Okada M, Imai Y, Kim T, et al. Comparison of enhancement patterns of histologically confirmed hepatocellular carcinoma between gadoxetate- and ferucarbotran-enhanced magnetic resonance imaging. J Magn Reson Imaging 2010;32(4):903–913.
7. Lee VS, Lavelle MT, Rofsky NM, et al. Hepatic MR imaging with a dynamic contrast-enhanced isotropic volumetric interpolated breath-hold examination: feasibility, reproducibility, and technical quality. Radiology 2000;215(2):365–372.
8. Golfieri R, Renzulli M, Lucidi V, Corcioni B, Trevisani F, Bolondi L. Contribution of the hepatobiliary phase of Gd-EOB-DTPA-enhanced MRI to Dynamic MRI in the detection of hypovascular small (≤ 2 cm) HCC in cirrhosis. Eur Radiol 2011;21(6):1233–1242.
9. International Consensus Group for Hepatocellular NeoplasiaThe International Consensus Group for Hepatocellular Neoplasia. Pathologic diagnosis of early hepatocellular carcinoma: a report of the international consensus group for hepatocellular neoplasia. Hepatology 2009;49(2):658–664.
10. Hayashi M, Matsui O, Ueda K, et al. Correlation between the blood supply and grade of malignancy of hepatocellular nodules associated with liver cirrhosis: evaluation by CT during intraarterial injection of contrast medium. AJR Am J Roentgenol 1999;172(4):969–976.
11. Yu JS, Chung JJ, Kim JH, Kim KW. Fat-containing nodules in the cirrhotic liver: chemical shift MRI features and clinical implications. AJR Am J Roentgenol 2007;188(4):1009–1016.
12. Motosugi U, Ichikawa T, Sano K, et al. Outcome of hypovascular hepatic nodules revealing no gadoxetic acid uptake in patients

with chronic liver disease. J Magn Reson Imaging 2011;34(1):88–94.

13. Kumada T, Toyoda H, Tada T, et al. Evolution of hypointense hepatocellular nodules observed only in the hepatobiliary phase of gadoxetate disodium-enhanced MRI. AJR Am J Roentgenol 2011;197(1):58–63.
14. Sakamoto M, Hirohashi S, Shimosato Y. Early stages of multistep hepatocarcinogenesis: adenomatous hyperplasia and early hepatocellular carcinoma. Hum Pathol 1991;22(2):172–178.
15. Makuuchi M, Kokudo N, Arii S, et al. Development of evidence-based clinical guidelines for the diagnosis and treatment of hepatocellular carcinoma in Japan. Hepatol Res 2008;38(1):37–51.
16. Kagawa Y, Okada M, Kumano S, et al. Optimal scanning protocol of arterial dominant phase for hypervascular hepatocellular carcinoma with gadolinium-ethoxybenzyl-diethylenetriamine pentaacetic acid-enhanced MR. J Magn Reson Imaging 2011;33(4):864–872.
17. Goshima S, Kanematsu M, Kondo H, et al. MDCT of the liver and hypervascular hepatocellular carcinomas: optimizing scan delays for bolus-tracking techniques of hepatic arterial and portal venous phases. AJR Am J Roentgenol 2006;187(1):W25–W32.
18. Hori M, Murakami T, Kim T, Nakamura H. Diagnosis of hepatic neoplasms using CT arterial portography and CT hepatic arteriography. Tech Vasc Interv Radiol 2002; 5(3):164–169.
19. Kudo M, Hatanaka K, Maekawa K. Newly developed novel ultrasound technique, defect reperfusion ultrasound imaging, using sonazoid in the management of hepatocellular carcinoma. Oncology 2010;78(Suppl 1):40–45.
20. Collins VP, Loeffler RK, Tivey H. Observations on growth rates of human tumors. Am J Roentgenol Radium Ther Nucl Med 1956;76(5):988–1000.
21. Schwartz M. A biomathematical approach to clinical tumor growth. Cancer 1961; 14:1272–1294.
22. R Development Core Team. R: A language and environment for statistical computing. Vienna, Austria: R Foundation for Statistical Computing, 2010.
23. Lin DY. Cox regression analysis of multivariate failure time data: the marginal approach. Stat Med 1994;13(21):2233–2247.
24. Fawcett T. An introduction to ROC analysis. Pattern Recognit Lett 2006;27(8):861–874.
25. Kadoya M, Matsui O, Takashima T, Nonomura A. Hepatocellular carcinoma: correlation of MR imaging and histopathologic findings. Radiology 1992;183(3):819–825.
26. Ohtomo K, Baron RL, Dodd GD 3rd, Federle MP, Ohtomo Y, Confer SR. Confluent hepatic fibrosis in advanced cirrhosis: evaluation with MR imaging. Radiology 1993;189(3):871–874.
27. Kim T, Baron RL, Nalesnik MA. Infarcted regenerative nodules in cirrhosis: CT and MR imaging findings with pathologic correlation. AJR Am J Roentgenol 2000;175(4): 1121–1125.
28. Hussain HK, Syed I, Nghiem HV, et al. T2-weighted MR imaging in the assessment of cirrhotic liver. Radiology 2004;230(3): 637–644.
29. Fattovich G, Stroffolini T, Zagni I, Donato F. Hepatocellular carcinoma in cirrhosis: incidence and risk factors. Gastroenterology 2004;127(5,Suppl 1):S35–S50.
30. Bolondi L, Sofia S, Siringo S, et al. Surveillance programme of cirrhotic patients for early diagnosis and treatment of hepatocellular carcinoma: a cost effectiveness analysis. Gut 2001;48(2):251–259.
31. Rozario R, Ramakrishna B. Histopathological study of chronic hepatitis B and C: a comparison of two scoring systems. J Hepatol 2003;38(2):223–229.
32. Matsumoto A, Tanaka E, Rokuhara A, et al. Efficacy of lamivudine for preventing hepatocellular carcinoma in chronic hepatitis B: A multicenter retrospective study of 2795 patients. Hepatol Res 2005;32(3): 173–184.
33. Kobayashi S, Matsui O, Gabata T, et al. Gadolinium ethoxybenzyl diethylenetriamine pentaacetic Acid-enhanced magnetic resonance imaging findings of borderline lesions at high risk for progression to hypervascular classic hepatocellular carcinoma. J Comput Assist Tomogr 2011;35(2): 181–186.
34. Ebara M, Fukuda H, Kojima Y, et al. Small hepatocellular carcinoma: relationship of signal intensity to histopathologic findings and metal content of the tumor and surrounding hepatic parenchyma. Radiology 1999; 210(1):81–88.
35. Basaran C, Karcaaltincaba M, Akata D, et al. Fat-containing lesions of the liver: cross-sectional imaging findings with emphasis on MRI. AJR Am J Roentgenol 2005; 184(4):1103–1110.
36. Jeong YY, Mitchell DG, Kamishima T. Small (<20 mm) enhancing hepatic nodules seen on arterial phase MR imaging of the cirrhotic liver: clinical implications. AJR Am J Roentgenol 2002;178(6):1327–1334.
37. Bruix J, Sherman M; Practice Guidelines Committee, American Association for the Study of Liver Diseases. Management of hepatocellular carcinoma. Hepatology 2005;42(5):1208–1236.
38. Zech CJ, Vos B, Nordell A, et al. Vascular enhancement in early dynamic liver MR imaging in an animal model: comparison of two injection regimen and two different doses Gd-EOB-DTPA (gadoxetic acid) with standard Gd-DTPA. Invest Radiol 2009;44(6):305–310.
39. Chung SH, Kim MJ, Choi JY, Hong HS. Comparison of two different injection rates of gadoxetic acid for arterial phase MRI of the liver. J Magn Reson Imaging 2010;31(2):365–372.
40. Kim KA, Herigault G, Kim MJ, Chung YE, Hong HS, Choi SY. Three-dimensional contrast-enhanced hepatic MR imaging: comparison between a centric technique and a linear approach with partial Fourier along both slice and phase directions. J Magn Reson Imaging 2011;33(1):160–166.

Liver INTERNATIONAL
OFFICIAL JOURNAL OF THE INTERNATIONAL ASSOCIATION FOR THE STUDY OF THE LIVER

Liver International ISSN 1478-3223

BASIC STUDIES

A glycyrrhizin-containing preparation reduces hepatic steatosis induced by hepatitis C virus protein and iron in mice

Masaaki Korenaga[1], Isao Hidaka[2], Sohji Nishina[1], Aya Sakai[3], Akane Shinozaki[3], Toshikazu Gondo[4], Takakazu Furutani[5], Hiroo Kawano[6], Isao Sakaida[2] and Keisuke Hino[1]

1 Department of Hepatology and Pancreatology, Kawasaki Medical University, Okayama, Japan
2 Department of Gastroenterology and Hepatology, Yamaguchi University Graduate School of Medicine, Yamaguchi, Japan
3 Department of Basic Laboratory Sciences, Yamaguchi University Graduate School of Medicine, Yamaguchi, Japan
4 Department of Surgical Pathology, Yamaguchi University Hospital, Yamaguchi, Japan
5 Department of Gastroenterology and Hepatology, Shuto General Hospital, Yamaguchi, Japan
6 Department of Pathology, Yamaguchi University Graduate School of Medicine, Yamaguchi, Japan

Keywords
carnitine palmitoyl transferase – mitochondria – oxidative stress – reactive oxygen species – transgenic mice

Abbreviations
ALT, alanine aminotransferase; ATF6, activating transcription factor 6; CCl_4, carbon tetrachloride; CHOP, CCAAT/enhancer-binding protein homology protein; CPT, carnitine palmitoyl transferase; ER, endoplasmic reticulum; FAS, fatty acid synthetase; γ-GCS, γ-glutamylcysteine synthetase; GSH, reduced glutathione; HCC, hepatocellular carcinoma; HCV, hepatitis C virus; IRE1, inositol-requiring enzyme 1; NAC, *N*-acetyl cysteine; PERK, PKR-like ER kinase; p-eIF2α, phosphorylated eukaryotic initiation factor-2α; PKR, RNA-activated protein kinase; ROS, reactive oxygen species; RT-PCR, reverse-transcription polymerase chain reaction; SNMC, Stronger Neo-Minophagen C; SREBP1, sterol regulatory element-binding protein 1; XBP-1, X-box DNA-binding protein 1.

Correspondence
Keisuke Hino, MD, PhD, Department of Hepatology and Pancreatology, Kawasaki Medical University, 577 Matsushima, Kurashiki, Okayama 701-0192, Japan
Tel: +81-86-4621111
Fax: +81-86-4641196
e-mail: khino@med.kawasaki-m.ac.jp

Received 1 July 2010
Accepted 7 January 2011

DOI:10.1111/j.1478-3231.2011.02469.x

Abstract

Background/Aim: A European randomized trial showed biochemical effects of 6-month treatment with Stronger Neo-Minophagen C™ (SNMC), a glycyrrhizin-containing preparation, in patients with chronic hepatitis C, but its underlying mechanisms remain elusive. We reported previously that SNMC exhibits an anti-oxidative effect in hepatitis C virus (HCV) transgenic mice that develop marked hepatic steatosis with mitochondrial injury under iron overloading. Hepatic steatosis and iron overload are oxidative stress-associated pathophysiological features in chronic hepatitis C. The aim of this study was to investigate whether long-term treatment with SNMC could prevent the development of hepatic steatosis in iron-overloaded HCV transgenic mice. *Methods:* C57BL/6 transgenic mice expressing the HCV polyprotein were fed an excess iron diet concomitantly with intraperitoneal injection of saline, SNMC, or seven-fold-concentrated SNMC thrice weekly for 6 months. *Results:* Stronger Neo-Minophagen C™ inhibited the development of hepatic steatosis in a dose-dependent manner without affecting hepatic iron content, attenuated ultrastructural alterations of mitochondria of the liver, activated mitochondrial β-oxidation with increased expression of carnitine palmitoyl transferase I and decreased the production of reactive oxygen species in the liver in iron-overloaded transgenic mice. However, SNMC hardly affected the unfolded protein response, which post-transcriptionally activates sterol regulatory element-binding protein 1, a transcription factor involved in lipid synthesis, even though we reported previously the activation of the unfolded protein response in the same iron-overloaded transgenic mice. *Conclusions:* These results suggest that SNMC prevents hepatic steatosis possibly by protecting mitochondria against oxidative stress induced by HCV proteins and iron overload.

Hepatitis C virus (HCV) causes acute and chronic hepatitis, cirrhosis and hepatocellular carcinoma (HCC) (1). Because current antiviral treatment can only eliminate the virus in approximately 50% of patients (2), therapies to reduce disease progression in chronically infected individuals would be of great benefit. In Japan, Stronger Neo-Minophagen C™ (SNMC), a glycyrrhizin-containing preparation, has been used as a treatment for

chronic hepatitis for more than 30 years. SNMC contained glycyrrhizin as the main active ingredient at first, and later a change was made in its composition on the basis of pharmacological studies including animal experiments and clinical studies. Currently, it is available in an injectable form for intravenous administration, containing 0.2% glycyrrhizin, 0.1% L-cystein and 2.0% glycine in physiological solution. A recent European randomized trial showed biochemical effects of 26-week treatment with SNMC in patients with chronic hepatitis C (3). In addition, Arase *et al.* (4) demonstrated that long-term usage of SNMC was effective in preventing HCC development in Japanese patients with chronic hepatitis C. However, the mechanisms by which SNMC prevents disease progression of chronic hepatitis C remain elusive.

Oxidative stress has been proposed to be one of the mechanisms of liver injury in HCV-associated chronic liver diseases (5), and hepatic steatosis and/or mitochondrial injury are well-known features in chronic hepatitis C (6, 7). We reported that HCV transgenic mice fed an excess iron diet show marked steatosis and mitochondrial injury at 6 months, and an increase in the hepatic lipid peroxidation products and the subsequent development of HCC at 12 months after the initiation of feeding (8). We also showed that a single injection of SNMC protected hepatocytes against carbon tetrachloride (CCl_4)-induced oxidative stress and mitochondrial injury in these transgenic mice without iron overload (9). These results prompted us to investigate whether SNMC inhibited the development of hepatic steatosis in terms of prevention of disease progression in chronic hepatitis C. The aim of this study was to examine whether long-term treatment with SNMC could prevent the development of hepatic steatosis in HCV transgenic mice fed an excess iron diet. In the present study, we show that SNMC reduces hepatic steatosis induced by HCV protein and iron overload in mice by means of a protective effect against mitochondrial injury.

Materials and methods

Animals and experimental design

The transgene pAlbSVPA-HCV, containing the full-length polyprotein-coding region under the control of the murine albumin promoter/enhancer, was described in detail (10, 11). Of the four transgenic lineages with evidence of RNA transcription of the full-length HCV-N open reading frame (FL-N), the FL-N/35 lineage proved capable of breeding in large numbers. There is no inflammation in the transgenic liver (11). Male FL-N/35 transgenic mice were fed an excess iron diet (carbonyl iron 225 mg/kg diet) at the age of 8 weeks, injected intraperitoneally with 50 μl of saline (control), SNMC or seven-fold-concentrated SNMC (supplied by Minophagen Pharmaceutical Co. Ltd, Tokyo, Japan) three times weekly and killed by intraperitoneal injection of 10% pentbarbital sodium preceded by 12-h fasting at 6 months after initiation of feeding according to the criteria outlined in the Guide for the Care and Use of Laboratory Animals.

Histological procedures

A portion of liver tissue was immediately snap frozen in liquid nitrogen for RNA extraction, protein extraction and determination of hepatic triglyceride and iron concentrations. The remaining liver tissue was fixed in 4% paraformaldehyde in phosphate-buffered saline and embedded in paraffin for histological analysis. Liver sections were stained with haematoxylin and eosin and Masson's trichrome method for fibrosis.

Hepatic triglyceride content

Lipids were extracted from the homogenized liver tissue by the method of Bligh and Dyer (12). The triglyceride levels were measured with a TGE test Wako kit (Wako Pure Chemicals, Tokyo, Japan), according to the manufacturer's instructions. Protein concentrations in liver were determined by the method of Lowry *et al.* (13), using a DC protein assay kit (Bio-Rad Laboratories, Hercules, CA, USA).

Hepatic iron concentration and hepcidin mRNA

The iron concentration in the liver was measured by atomic absorption spectrometry (Hitachi Z-6100, Tokyo, Japan), as described previously (8), and expressed as micrograms Fe/g of tissue (wet weight). One-step real-time reverse-transcription polymerase chain reaction was also performed as described previously (8). The primers amplifying the genes coding hepcidin and β-actin were as follows: hepcidin, sense; TCCTGCTTCTCCTCCTTGCC, antisense; GTCTGCCCTGCTTTCTTCCC (GenBank accession number, NM_032541) and β-actin, sense; TGACAGGATGCAGAAGGAGA, antisense; GCTGGAA GGTGGACAGTGAG (GenBank accession number, NM_ 007393).

Immunoblotting

Lysates of liver were separated by sodium dodecyl sulphate–polyacrylamide gel electrophoresis. The proteins were transferred to polyvinylidene difluoride membranes (Millipore, Bedford, MA, USA), blocked overnight at 4 °C with 5% skim milk and 0.1% Tween 20 in Tris-buffered saline, and subsequently incubated for 1 h at room temperature with an anti-rabbit carnitine palmitoyl transferase I (CPTI) antibody, anti-rabbit CPTII antibody (Alpha Diagnostic International, San Antonio, TX, USA), anti-rabbit sterol regulatory element-binding protein 1 (SREBP1) antibody (Santa Cruz Biotechnology Inc., Santa Cruz, CA, USA), anti-rabbit fatty acid synthetase (FAS) antibody (Cell Signaling Technology Inc., Boston, MA, USA), anti-mouse X-box

DNA-binding protein 1 (XBP-1) antibody (Santa Cruz Biotechnology Inc.) or anti-bacterially expressed, mouse CCAAT/enhancer-binding protein homology protein (CHOP) fusion protein antibody (Abcam, Cambridge, UK). Exceptionally, the proteins were blocked for 1 h at room temperature and subsequently incubated overnight at 4 °C with an anti-rabbit phosphorylated eukaryotic initiation factor-2α (p-eIF2α) antibody (Cell Signaling Technology Inc.).

Electron microscopy

Liver specimens were fixed in 2.1% glutaraldehyde, post-fixed in 1% osmium tetroxide, dehydrated in graded ethanol and propylene dioxide and embedded in Epok. Thick sections (1 μm in width) were stained with toluidine blue to identify steatosis by light microscopy. Thin sections were stained with uranyl acetate and lead citrate, and examined using a Hitachi-7000 transmission electron microscope (Hitachi Ltd., Tokyo, Japan). The length of mitochondria was measured using IMAGE-PRO PLUS 4.0 software (Media Cybernetics Inc., Bethesda, MD, USA) for two randomly selected areas of electron microscopic images in each mice to quantify ultrastructural alterations of mitochondria.

In vivo formation of $[^{14}C]CO_2$ from [U-^{14}C] palmitic acid

A tracer dose of [U-^{14}C] palmitic acid (150 μCi/kg; 0.16 μmol/kg, American Biosciences, St Louis, MO, USA) was administered by gastric intubation in 0.2 ml of corn oil, preceded by fasting for 42 h, as described previously (8). The animal was then placed for 6 h in a small plastic cage swept by an airflow of 50 ml/min. The outflow was bubbled into 30 ml of monoethanolamine. After 6 h, 1 ml was removed and counted for $[^{14}C]$ CO_2 activity with an Aloka Liquid Scintillation Counter 5100 (Aloka Co. Ltd., Tokyo, Japan).

In situ detection of reactive oxygen species

In situ reactive oxygen species (ROS) production in the liver was assessed by staining with dihydroethidium as described previously (14). In the presence of ROS, dihydroethidium (Invitrogen Corp., Carlsbad, CA, USA) is oxidized to ethidium bromide and stains nuclei bright red by intercalating with the DNA (15). Fluorescence intensity was quantified using NIH image analysis software for three randomly selected areas of digital images for each mouse.

Statistical analysis

Quantitative values are expressed as mean ± SD. Two groups among multiple groups were compared by the rank-based, Kruskal–Wallis ANOVA test followed by the Scheffé test. Data between two groups were compared by Student's *t*-test. A P value of < 0.05 was considered to be significant.

Results

Serum alanine aminotransferase levels and hepatic triglyceride accumulation

Six-month treatment with SNMC or seven-fold-concentrated SNMC significantly reduced serum alanine aminotransferase (ALT) ($P < 0.05$) in FL-N/35 transgenic mice fed the excess iron diet (Fig. 1A). Transgenic mice fed the excess iron diet developed severe steatosis including the centrilobular microvesicular type, as described previously (8, 16). SNMC reduced hepatic triglyceride content in a dose-dependent manner ($P < 0.05$, $P < 0.01$, Fig. 1B). SNMC obviously reduced the centrilobular microvesicular steatosis and moderately decreased hepatic steatosis in the remaining areas of hepatic lobules, whereas seven-fold-concentrated SNMC almost completely suppressed hepatic steatosis (Fig. 1C). Mice in the three groups (control, SNMC and seven-fold-concentrated SNMC) showed no evidence of intrahepatic inflammation or fibrosis.

Hepatic iron content

We reported that iron overload reinforced hepatic steatosis in FL-N/35 transgenic mice (8). We first measured hepatic iron levels and the expression of hepcidin, a negative regulator in iron homeostasis, to assess whether SNMC attenuated hepatic iron overload. As shown in Figure 2, 6-month treatment with SNMC or seven-fold-concentrated SNMC changed neither the hepatic iron level nor the hepcidin expression in transgenic mice fed the excess iron diet, suggesting that SNMC inhibited hepatic steatosis without affecting iron overload.

Mitochondrial ultrastructure

As we observed previously the attenuation of CCl_4-induced ultrastructural alterations of mitochondria by SNMC in FL-N/35 transgenic mice (9), and found obvious reduction of centrilobular microvesicular steatosis by SNMC in the present study, we next examined the ultrastructure of the hepatic mitochondria in FL-N/35 transgenic mice fed the excess iron diet. Ultrastructural alterations such as irregularly sized mitochondria, swollen mitochondria or disorganized cristae that were observed in FL-N/35 transgenic mice fed the excess iron were much less frequently found after the 6-month treatment with SNMC in a dose-dependent manner (Fig. 3A–C). The mean length of mitochondria was significantly greater in mice without SNMC than in those with SNMC (Fig. 3D). Thus, SNMC attenuated ultrastructural alterations of mitochondria of the liver in FL-N/35 transgenic mice fed the excess iron diet.

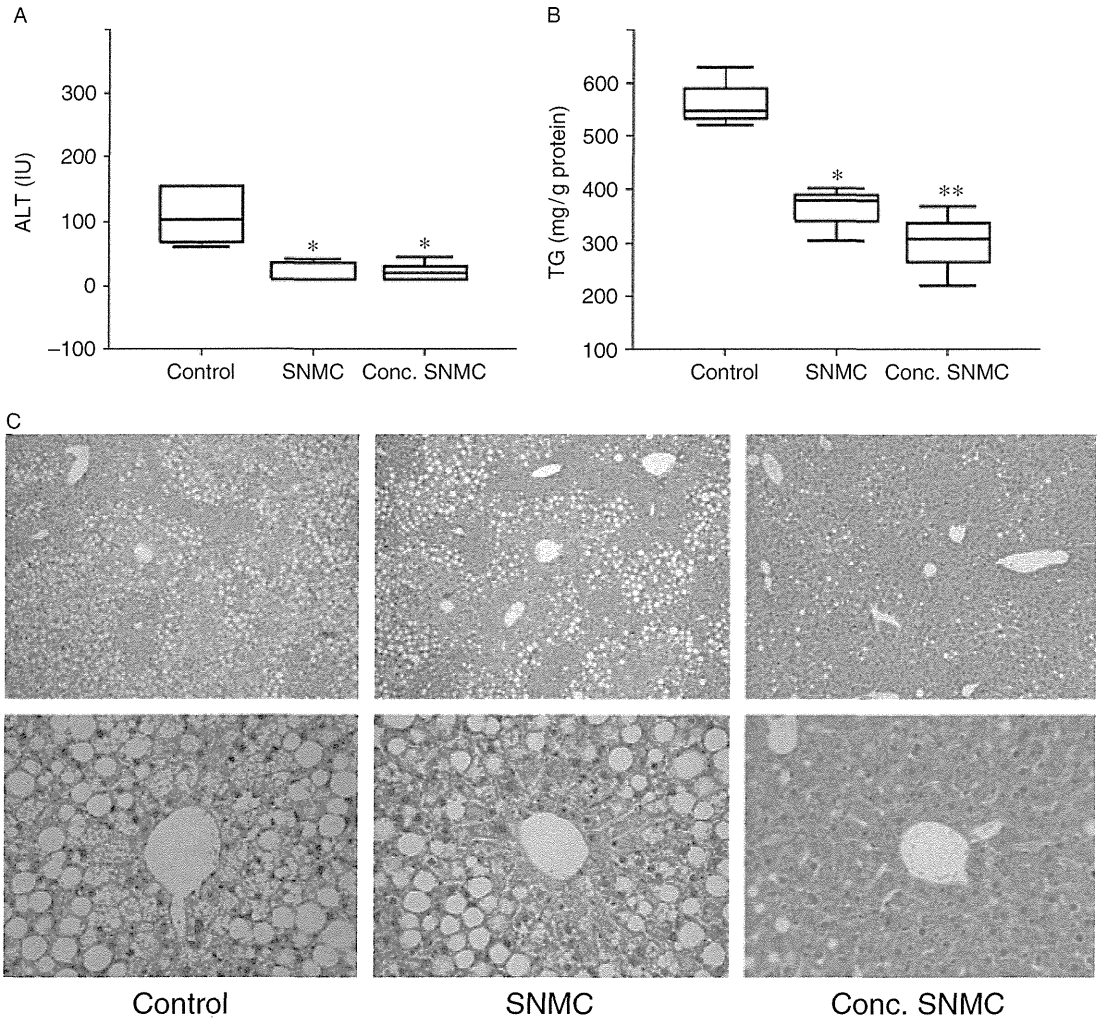

Fig. 1. Serum alanine aminotransferase (ALT) levels, hepatic triglyceride levels and hepatic steatosis in iron-overloaded FL-N/35 transgenic mice in three groups. (A) Serum ALT levels in six mice in each group. (B) Hepatic triglyceride levels in three mice in each group. ALT and triglyceride levels are shown as box plot profiles. The bottom and top edges of the boxes are the 25th and 75th percentiles respectively. The median value is shown by the line within the box. (C) Hepatic steatosis in mice in each group (haematoxylin and eosin, original magnification × 100 for upper panel and × 400 for lower panel). Control, transgenic mice injected intraperitoneally with 50 μl of saline three times weekly for 6 months; Stronger Neo-Minophagen C^{TM} (SNMC), transgenic mice injected intraperitoneally with 50 μl of SNMC three times weekly for 6 months; Conc. SNMC, transgenic mice injected intraperitoneally with 50 μl of seven-fold-concentrated SNMC three times weekly for 6 months. *$P < 0.05$, $P < 0.01$ vs control.

Degradation activity of fatty acid

We next examined *in vivo* formation of [^{14}C]CO_2 from [U-^{14}C] palmitic acid (C16:0) to assess whether SNMC improved mitochondrial function. Palmitic acid is a long-chain fatty acid. Mitochondria catalyse the β-oxidation of the bulk of short-, medium- and long-chain fatty acids (17). As shown in Figure 4A, SNMC significantly increased the *in vivo* formation of [^{14}C]CO_2 from [U-^{14}C] palmitic acid in FL-N/35 transgenic mice fed the excess iron diet ($P < 0.05$). These results suggested that SNMC improved mitochondrial β-oxidation activity.

Carnitine palmitoyl transferase I expression

Carnitine palmitoyl transferase I and CPTII regulate oxidation of long-chain fatty acids in the mitochondria. CPTI, a transmembrane enzyme of the mitochondrial outer membrane, has been shown to be the rate-limiting step in the β-oxidation of long-chain fatty acids (18). The expression of CPTI, but not CPTII, significantly increased after the 6-month treatment with SNMC or seven-fold-concentrated SNMC ($P < 0.005$, Fig. 4B). We reported previously the decreased expression of CPTI in FL-N/35 transgenic mice fed the excess iron diet as compared with nontransgenic mice fed the control diet

Liver International (2011)

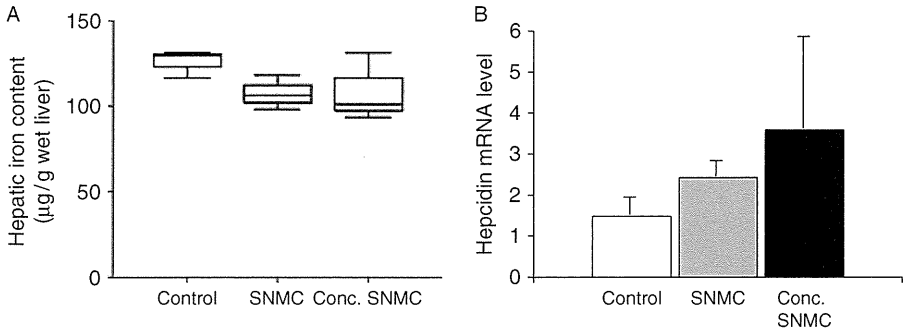

Fig. 2. Iron content and hepcidin mRNA expression in the liver in iron-overloaded FL-N/35 transgenic mice in each group. (A) Hepatic iron concentrations were measured by atomic absorption spectrometry in three mice in each group. The results are shown as box plot profiles. The bottom and top edges of the boxes are the 25th and 75th percentiles respectively. The median value is shown by the line within the box. (B) The expression levels of hepcidin mRNA was measured by reverse-transcription polymerase chain reaction in three mice in each group. The relative quantities of hepcidin mRNA were normalized to β-actin mRNA. Control, Stronger Neo-Minophagen C^{TM} (SNMC) and Conc. SNMC; see legend for Figure 1.

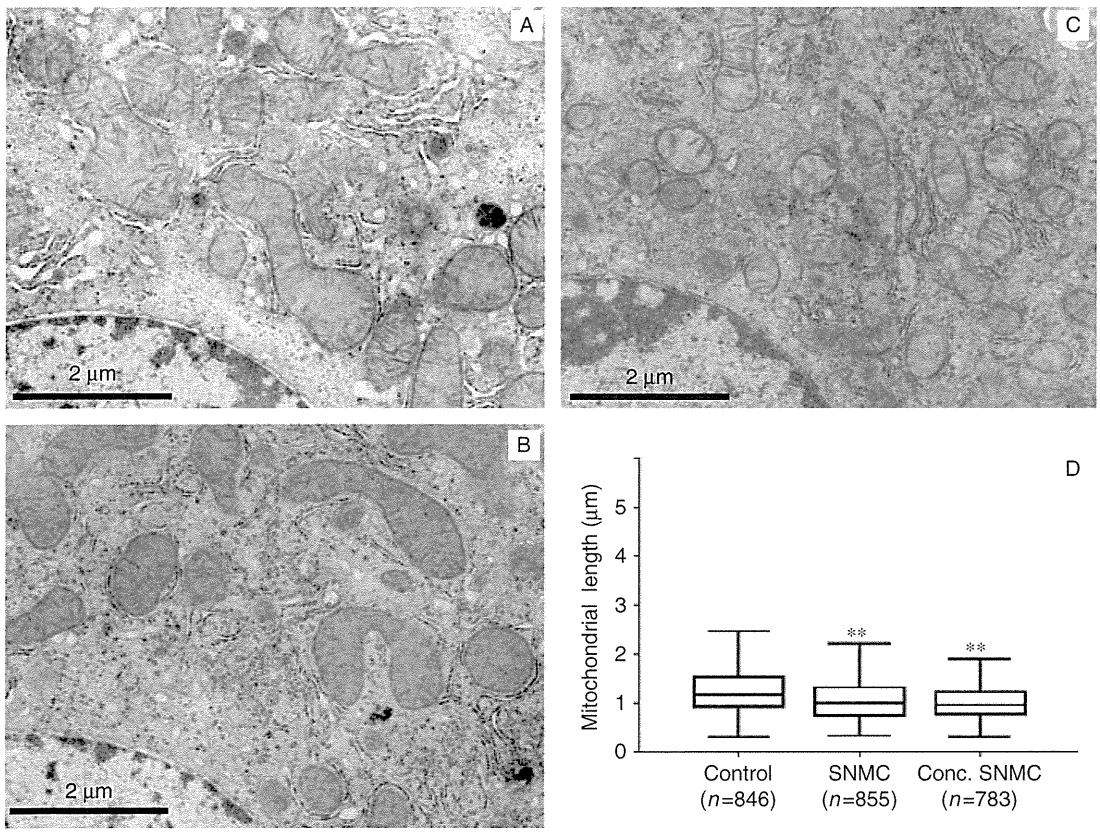

Fig. 3. Electron microscopy of the liver of an iron-overloaded FL-N/35 transgenic mouse from each group. Ultrastructural alterations such as irregularly sized mitochondria, swollen mitochondria and disorganized cristae that were observed in the iron-overloaded FL-N/35 transgenic mouse were much less frequently found after a 6-month treatment with Stronger Neo-Minophagen C^{TM} (SNMC) in a dose-dependent manner. The magnification scale is indicated in the left-lower corner of each picture. The length of mitochondria was assessed for three mice in each group and measured using IMAGE-PRO PLUS 4.0 software for two randomly selected areas of electron microscopic images in each mice. The numbers in parentheses represent the total number of mitochondria examined in each group. Control, SNMC and Conc. SNMC; see legend for Figure 1. (A) Control; (B) SNMC; (C) Conc. SNMC; and (D) the length of mitochondria. $^{**}P < 0.0001$ vs control.

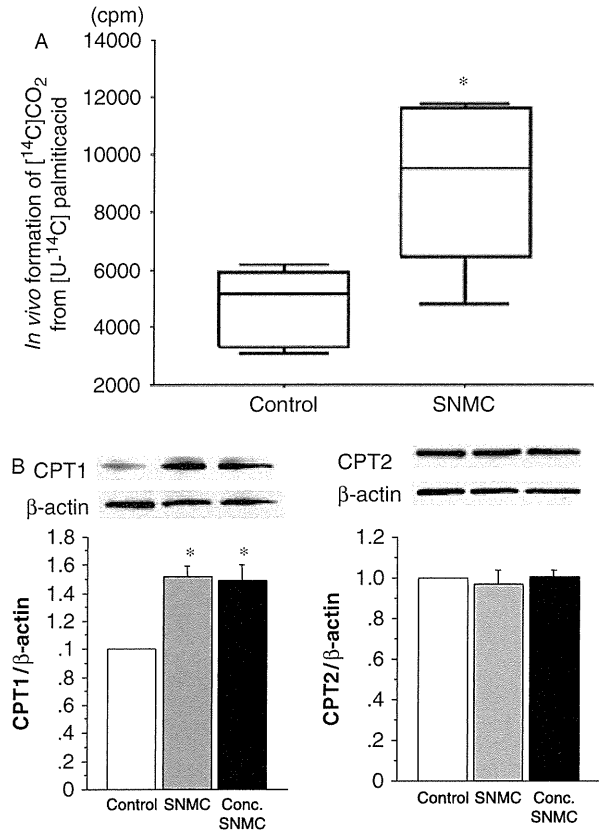

Fig. 4. *In vivo* formation of [^{14}C]CO_2 from [U-^{14}C] palmitic acid and hepatic expression of carnitine palmitoyl transferase I (CPTI) and CPTII in iron-overloaded FL-N/35 transgenic mice in each group. (A) A tracer dose of [U-^{14}C] palmitic acid (150 μCi/kg; 0.16 μmol/kg) was administered by gastric intubation in 0.2 ml of corn oil, preceded by fasting for 42 h. The animal was then placed for 6 h in a small plastic cage swept by an airflow of 50 ml/min. The outflow was bubbled into 30 ml of monoethanolamine. After 6 h, 1 ml was removed and counted for [^{14}C] CO_2 activity. This experiment was carried out for five mice in each group. The results are shown as box plot profiles. The bottom and top edges of the boxes are the 25th and 75th percentiles respectively. The median value is shown by the line within the box. (B) Immunoblots for CPTI and CPTII were performed using liver lysates from four mice in each group. The degree of protein expression was normalized with β-actin. Control, Stronger Neo-Minophagen C™ (SNMC) and Conc. SNMC; see legend for Figure 1. *$P < 0.05$ vs control.

(16), which may be related to the association of HCV core protein with the mitochondrial outer membrane (19). Together with improvement of the mitochondrial structure, β-oxidation activity and CPTI expression, SNMC had a protective effect against mitochondrial injury induced by HCV proteins and iron overload.

Reactive oxygen species production

We have reported previously that HCV core protein increases ROS production through inhibition of mitochondrial electron transport (19), and found increased ROS production in FL-N/35 transgenic mice fed the excess iron diet as compared with nontransgenic mice fed the control diet (16). Therefore, we evaluated *in situ* ROS production to assess whether SNMC reduces ROS production in the liver in terms of a protective effect against mitochondrial injury. ROS production was significantly reduced by SNMC in a dose-dependent manner ($P < 0.005$, $P < 0.001$, Fig. 5). Thus, SNMC reduced hepatic steatosis by protecting mitochondria against oxidative stress induced by HCV proteins and iron overload.

Unfolded protein response and sterol regulatory element-binding protein 1 expression

We next evaluated the effect of SNMC on the unfolded protein response and the expression of SREBP1, a transcription factor that activates genes required for lipogenesis (20), because we found in our previous study that not only the decreased CPTI expression but also the increased SREBP1 expression owing to the activated unfolded protein response contributed to the development of hepatic steatosis in FL-N/35 transgenic mice fed the excess iron diet (16). The unfolded protein response signalling cascades are initiated by three endoplasmic reticulum (ER)-resident sensors: inositol-requiring enzyme 1 (IRE1), RNA-activated protein kinase-like ER kinase (PERK) and activating transcription factor 6 (ATF6) (21). IRE1 activation splices unspliced XBP-1 (uXBP-1) to form spliced XBP-1 (sXBP-1) mRNA (22), and was assessed by the sXBP-1 protein level (23). PERK activation was evaluated by measurement of p-eIF2α and CHOP (24). ATF6 activation was assessed by uXBP-1 expression (25). Six-month treatment with SNMC or seven-fold-concentrated SNMC did not change the expression of sXBP-1, CHOP, SREBP1 or FAS, a target gene of SREBP1, but decreased the expression of uXBP-1 and p-eIF2α (Fig. 6). These results suggested that SNMC inhibited hepatic steatosis through a protective effect against mitochondrial injury rather than restoration of activated lipogenesis in FL-N/35 transgenic mice fed the excess iron diet, even though it may attenuate the unfolded protein response to some degree.

Discussion

Hepatic steatosis and iron overload are not only pathophysiological features of HCV-associated chronic liver disease (5, 26) but also risk factors for the development of HCC (27, 28). The present animal model, FL-N/35 transgenic mice fed an excess iron diet, had several similarities with patients having HCV-associated chronic liver disease in terms of development of hepatic steatosis, followed by hepatocarcinogenesis (8), even though hepatic steatosis in this model was different from one observed in patients with HCV genotype 3 infection as to whether it was virally induced. In addition, the hepatic

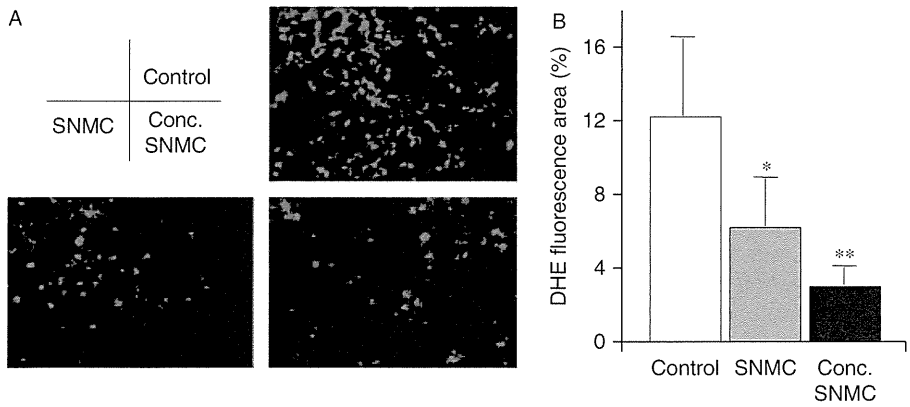

Fig. 5. Reactive oxygen species production in the liver in iron-overloaded FL-N/35 transgenic mice in each group. (A) Frozen liver sections of mice in each group were stained with dihydroethidium. (B) Fluorescence intensity was quantified by NIH image analysis software for three randomly selected areas of digital images for four mice in each group. Control, Stronger Neo-Minophagen C^{TM} (SNMC) and Conc. SNMC; see legend for Figure 1. $^{*}P < 0.005$ vs control, $^{**}P < 0.001$ vs control, $P < 0.05$ vs SNMC.

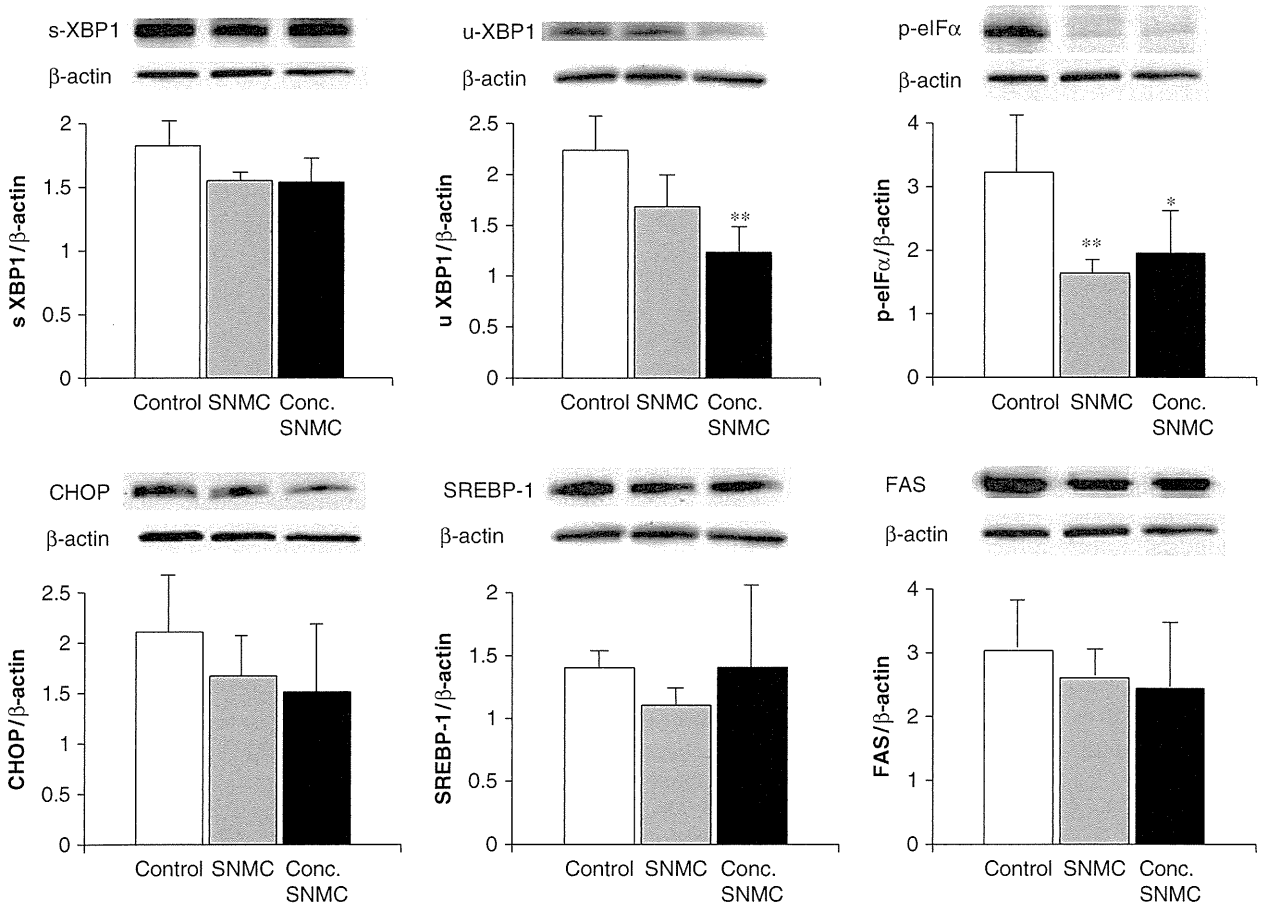

Fig. 6. Expression of spliced X-box DNA-binding protein 1 (sXBP-1), unspliced X-box DNA-binding protein 1 (uXBP-1), phosphorylated initiation factor-2α (p-IF2α), CCAAT/enhancer-binding protein homology protein (CHOP), sterol regulatory element-binding protein 1 (SREBP1) and fatty acid synthetase (FAS) in the liver in mice in each group. Immunoblots were performed using liver lysates from four mice in each group. The degree of protein expression was normalized with β-actin. Control, Stronger Neo-Minophagen C^{TM} (SNMC) and Conc. SNMC; see legend for Figure 1. $^{*}P < 0.05$ vs control, $^{**}P < 0.01$ vs control, $P < 0.05$ vs SNMC.

iron concentration of FL-N/35 transgenic mice fed the excess iron diet was comparable with that of a large number of patients with chronic hepatitis C in extensive studies (29, 30). Thus, FL-N/35 transgenic mice fed the excess iron diet appeared to be a suitable animal model to assess the effect of the long-term treatment with SNMC on the development of hepatic steatosis in HCV infection. The dose of SNMC administered to the FL-N/35 transgenic mice was comparable with the dosage given to patients with chronic hepatitis (approximately 100 ml of SNMC). This implies that a clinical dosage of SNMC has the potential to reduce hepatic steatosis occurring in patients with HCV-associated chronic liver diseases. There was no histological improvement such as inflammation or fibrosis regardless of serum ALT reduction in the human study, where the change of hepatic steatosis was not assessed (3). We could not evaluate whether SNMC has a potential to reduce inflammation or fibrosis in this study, because the present animal model did not show inflammation or fibrosis. Therefore, the decreased serum ALT levels in this model were thought to reflect the reduction of hepatic steatosis by SNMC.

Our previous study indicated that iron overload reinforced hepatic steatosis through ROS-induced activation of the unfolded protein response in FL-N/35 transgenic mice, and that an anti-oxidant, *N*-acetyl cysteine (NAC), almost completely blocked ROS production and cancelled hepatic steatosis induced by HCV proteins and iron (16). In the present study, SNMC reduced ROS production to a lesser degree than NAC. SNMC did not affect the hepatic iron content or hepcidin expression level, even though we reported previously the ROS-associated inhibition of hepcidin transcription in FL-N/35 transgenic mice (14). Nor did SNMC fully inhibit the ROS-associated unfolded protein response; nevertheless, SNMC effectively inhibited the development of hepatic steatosis in a dose-dependent manner through improvement of the mitochondrial structure, β-oxidation activity and CPTI expression. It should be noted that SNMC had a protective effect against mitochondrial injury rather than a simple anti-oxidative effect in FL-N/35 transgenic mice fed the excess iron.

Carnitine palmitoyl transferase I is negatively regulated by malonyl-CoA, an intermediate product in fatty acid synthesis, at the transcriptional level (18). Therefore, we need to consider at least two explanations for the increased CPTI expression induced by the 6-month treatment with SNMC. HCV core protein has been shown to be located on the mitochondrial outer membrane (19, 31), which may damage the membrane. One explanation is that SNMC increases CPTI expression through the restoration of the damaged mitochondrial outer membrane, as shown by the attenuated ultrastructural alterations of mitochondria with SNMC in FL-N/35 transgenic mice fed the excess iron. Another explanation is that SNMC may increase CPTI expression through the inhibition of fatty acid synthesis. However, the latter explanation seems unlikely, because the 6-month treatment with SNMC did not change the expression of SREBP1 or FAS (Fig. 6). Thus, the mechanisms by which SNMC reduces hepatic steatosis induced by HCV protein and iron overload may be mainly because of increased β-oxidation activity associated with increased CPTI stability through the protective effect against mitochondrial injury.

Of particular concern is how SNMC exerts its protective effect against mitochondrial injury. We reported previously that SNMC restored depletion of reduced glutathione (GSH) induced by CCl_4 and increased the synthesis of γ-glutamylcysteine synthetase (γ-GCS), a rate-limiting enzyme regulating GSH synthesis, at the transcriptional level in FL-N/35 transgenic mice (9). Judging from the protective effect of SNMC against mitochondrial injury, SNMC may play a role in the reduction of mitochondrial oxidative stress. Hepatic GSH synthesis is mainly regulated by the availability of cysteine, the sulphur amino acid precursor and the activity of γ-GCS. SNMC consists of 0.2 glycyrrhizin, 0.1 cycteine and 2.0% glycine in physiological solution. The cysteine included in SNMC may also contribute to GSH synthesis through its increased availability. The present study was largely observational and therefore further analysis is needed to clarify the mechanisms by which SNMC exerts a protective effect against mitochondrial injury.

In conclusion, this study shows that SNMC reduces hepatic steatosis induced by HCV protein and iron overload in mice by inducing increased β-oxidation activity associated with an increased CPTI expression.

Acknowledgements

This study was supported by a grant from the Ministry of Education, Culture, Sports, Science and Technology (No. 20590782), and in part by a Research on Hepatitis, Health and Labour Sciences Research Grants from the Ministry of Health, Labor and Welfare, Japan.

References

1. Seeff LB. Natural history of chronic hepatitis C. *Hepatology* 2002; **36**: S35–46.
2. Fried MW, Shiffman ML, Reddy KR, *et al.* Peginterferon alfa-2a plus ribavirin for chronic hepatitis C virus infection. *N Engl J Med* 2002; **347**: 975–82.
3. Orlent H, Hansen BE, Willems M, *et al.* Biochemical and histological effects of 26 weeks of glycyrrhizin treatment in chronic hepatitis C: a randomized phase II trial. *J Hepatol* 2006; **45**: 539–46.
4. Arase Y, Ikeda K, Murashima N, *et al.* The long term efficacy of glycyrrhizin in chronic hepatitis C patients. *Cancer* 1997; **79**: 1494–500.
5. Farinati F, Cardin R, De Maria N, *et al.* Iron storage, lipid peroxidation and glutathione turnover in chronic anti-HCV positive hepatitis. *J Hepatol* 1995; **22**: 449–56.

6. Kitase A, Hino K, Furutani T, *et al.* In situ detection of oxidized n-3 polyunsaturated fatty acids in chronic hepatitis C: correlation with hepatic steatosis. *J Gastroenterol* 2005; **40**: 617–24.
7. Barbaro G, Di Lorenzo G, Asti A, *et al.* Hepatocellular mitochondrial alterations in patients with chronic hepatitis C: ultrastructural and biochemical findings. *Am J Gastroenterol* 1999; **94**: 2198–205.
8. Furutani T, Hino K, Okuda M, *et al.* Hepatic iron overload induces hepatocellular carcinoma in transgenic mice expressing the hepatitis C virus polyprotein. *Gastroenterology* 2006; **130**: 2087–98.
9. Hidaka I, Hino K, Korenaga M, *et al.* Stronger Neo-Minophagen C^{TM}, a glycyrrhizin-containing preparation, protects liver against carbon tetrachloride-induced oxidative stress in transgenic mice expressing the hepatitis C virus polyprotein. *Liver Int* 2007; **27**: 845–53.
10. Beard MR, Abell G, Honda M, *et al.* An infectious molecular clone of a Japanese genotype 1b hepatitis C virus. *Hepatology* 1999; **30**: 316–24.
11. Lerat H, Honda M, Beard MR, *et al.* Steatosis and liver cancer in transgenic mice expressing the structural and nonstructural proteins of hepatitis C virus. *Gastroenterology* 2002; **122**: 352–65.
12. Bligh EG, Dyer WJ. A rapid method of total lipid extraction and purification. *Can J Biochem Physiol* 1959; **37**: 911–7.
13. Lowry OH, Rosebrough NJ, Farr AL, Randall RJ. Protein measurement with the Folin phenol reagent. *J Biol Chem* 1951; **193**: 265–75.
14. Nishina S, Hino K, Korenaga M, *et al.* Hepatitis C virus-induced reactive oxygen species raise hepatic iron level in mice by reducing hepcidin transcription. *Gastroenterology* 2008; **134**: 226–38.
15. Harrison-Findik DD, Schafer D, Klein E, *et al.* Alcohol metabolism-mediated oxidative stress down-regulates hepcidin transcription and leads to increased duodenal iron transporter expression. *J Biol Chem* 2006; **281**: 22974–82.
16. Nishina S, Korenaga M, Hino K, *et al.* Hepatitis C virus protein and iron overload induce hepatic steatosis through the unfolded protein response in mice. *Liver Int* 2010; **30**: 683–92.
17. Rao MS, Reddy JK. Peroxisomal beta-oxidation and steatohepatitis. *Semin Liver Dis* 2001; **21**: 43–55.
18. Kerner J, Hoppel C. Fatty acid import into mitochondria. *Biochim Biophys Acta* 2000; **1486**: 1–17.
19. Korenaga M, Wang T, Li Y, *et al.* Hepatitis C virus core protein inhibits mitochondrial electron transport and increases reactive oxygen species (ROS) production. *J Biol Chem* 2005; **280**: 37481–8.
20. Horton JD, Goldstein JL, Brown MS. SREBPs: activators of the complete program of cholesterol and fatty acid synthesis in the liver. *J Clin Invest* 2002; **109**: 1125–31.
21. Ji C, Kaplowitz N. ER stress: can the liver cope? *J Hepatol* 2006; **45**: 321–33.
22. Calfon M, Zeng H, Urano F, *et al.* IRE1 couples endoplasmic reticulum load to secretory capacity by processing the XBP-1 mRNA. *Nature* 2002; **415**: 92–6.
23. Yoshida H, Matsui T, Yamamoto A, Okada T, Mori K. XBP1 mRNA is induced by ATF6 and spliced by IRE1 in response to ER stress to produce a highly active transcription factor. *Cell* 2001; **107**: 881–91.
24. Marciniak SJ, Ron D. Endoplasmic reticulum stress signaling in disease. *Physiol Rev* 2006; **86**: 1133–49.
25. Okada T, Yoshida H, Akazawa R, Negishi M, Mori K. Distinct roles of activating transcription factor 6 (ATF6) and double-stranded RNA-activated protein kinase-like endoplasmic reticulum kinase (PERK) in transcription during the mammalian unfolded protein response. *Biochem J* 2002; **366**: 585–94.
26. Scheuer PJ, Ashrafzadeh P, Sherlock S, Brown D, Dusheiko GM. The pathology of hepatitis C. *Hepatology* 1992; **15**: 567–71.
27. Ohata K, Hamasaki K, Toriyama K, *et al.* Hepatic steatosis is a risk factor for hepatocellular carcinoma in patients with chronic hepatitis C virus infection. *Cancer* 2003; **97**: 3036–43.
28. Kato J, Kobune M, Nakamura T, *et al.* Normalization of elevated hepatic 8-hydroxy-2′-deoxyguanosine levels in chronic hepatitis C patients by phlebotomy and low iron diet. *Cancer Res* 2001; **61**: 8697–702.
29. Hofer H, Osterreicher C, Jessner W, *et al.* Hepatic iron concentration does not predict response to standard and pegylated-IFN/ribavirin therapy in patients with chronic hepatitis C. *J Hepatol* 2004; **40**: 1018–22.
30. Rulyak SJ, Eng SC, Patel K, *et al.* Relationships between hepatic iron content and virologic response in chronic hepatitis C patients treated with interferon and ribavirin. *Am J Gastroenterol* 2005; **100**: 332–7.
31. Schwer B, Ren S, Pietschmann T, *et al.* Targeting of hepatitis C virus core protein to mitochondria through a novel C-terminal localization motif. *J Virol* 2004; **78**: 7958–68.

Journal of Gastroenterology and Hepatology

A novel des-γ-carboxy prothrombin in serum for the diagnosis of hepatocellular carcinoma.

Journal:	*Journal of Gastroenterology and Hepatology*
Manuscript ID:	JGH-01249-2012.R1
Manuscript Type:	Original Article - Hepatology (Clinical)
Date Submitted by the Author:	n/a
Complete List of Authors:	Tanaka, Takahiro; Institutes of Health Biosciences, University of Tokushima Graduate School, Department of Gastroenterology and Oncology Taniguchi, Tatsuya; Institutes of Health Biosciences, University of Tokushima Graduate School, Department of Gastroenterology and Oncology Sannomiya, Katsutaka; Institutes of Health Biosciences, University of Tokushima Graduate School, Department of Gastroenterology and Oncology Takenaka, Hidetaka; Institutes of Health Biosciences, University of Tokushima Graduate School, Department of Gastroenterology and Oncology Tomonari, Tetsu; Institutes of Health Biosciences, University of Tokushima Graduate School, Department of Gastroenterology and Oncology Okamoto, Koichi; Institutes of Health Biosciences, University of Tokushima Graduate School, Department of Gastroenterology and Oncology Kitamura, Shinji; Institutes of Health Biosciences, University of Tokushima Graduate School, Department of Gastroenterology and Oncology Okahisa, Toshiya; Institutes of Health Biosciences, University of Tokushima Graduate School, Department of Gastroenterology and Oncology Tamaki, Katsuyoshi; Institutes of Health Biosciences, University of Tokushima Graduate School, Department of Gastroenterology and Oncology Mikasa, Hiroaki; Faculty of Medicine, Tokushima University, Medical Education Support Center Suzuki, Sadao; Nagoya City University Graduate School of Medical Sciences, Department of Public Health Takayama, Tetsuji; Institutes of Health Biosciences, University of Tokushima Graduate School, Department of Gastroenterology and Oncology
Key Words:	Hepatocellular carcinoma, clinical < Hepatology, Cell and molecular biology < Hepatology, Hepatocellar carcinoma, treatment < Hepatology